CM²

MAGAZINE

第 52 期

创刊词

　　海洋是生命的摇篮，是文明的纽带。地球上最早的生命诞生于海洋，海洋里的生命最终进化成了人类，人类的文化融合又通过海洋得以实现。人因海而兴。

　　人类对海洋的探索从未停止。从远古时代美丽的神话传说，到麦哲伦的全球航行，再到现代对大洋的科学钻探计划，海洋逐渐从人类敬畏崇拜幻想的精神寄托演变成可以开发利用与科学研究的客观存在。其中，上个世纪与太空探索同步发展的大洋科学钻探计划将人类对海洋的认知推向了崭新的纬度：深海（deep sea）与深时（deep time）。大洋钻探计划让人类知道，奔流不息的大海之下，埋藏的却是亿万年的地球历史。它们记录了地球板块的运动，从而使板块构造学说得到证实；它们记录了地球环境的演变，从而让古海洋学方兴未艾。

　　在探索海洋的悠久历史中，从大航海时代的导航，到大洋钻探计划中不可或缺的磁性地层学，磁学发挥了不可替代的作用。这不是偶然，因为从微观到宏观，磁性是最基本的物理属性之一，可以说，万物皆有磁性。基于课题组的学科背景和对海洋的理解，我们对海洋的探索以磁学为主要手段，海洋磁学中心因此而生。

　　海洋磁学中心，简称 CM²，一为其全名"Centre for Marine Magnetism"的缩写，另者恰与爱因斯坦著名的质能方程 $E = MC^2$ 对称，借以表达我们对科学巨匠的敬仰和对科学的不懈追求。

　　然而科学从来不是单打独斗的产物。我们以磁学为研究海洋的主攻利器，但绝不仅限于磁学。凡与磁学相关的领域均是我们关注的重点。为了跟踪反映国内外地球科学特别是与磁学有关的地球科学领域的最新研究进展，海洋磁学中心特地主办 CM² Magazine，以期与各位地球科学工作者相互交流学习、合作共进！

　　"海洋孕育了生命，联通了世界，促进了发展"。21 世纪是海洋科学的时代，由陆向海，让我们携手迈进中国海洋科学的黄金时代！

目 录

磁学演绎

第 42 章 海洋沉积物

　　磁性矿物主要以碎屑颗粒的形式由风、水或者冰川搬到海洋中（Henshaw and Merrill, 1980; Evans and Heller, 2003）。目前，河流供给是海洋沉积物的主要来源，约 20,000 Tg/yr（表 1），而冰川和风搬运来的碎屑沉积物相对较少，分别为 2,900 和 1,100 Tg/yr（表 1），还有其他供给如沿岸剥蚀和宇宙尘埃，沿岸剥蚀供给约 200 Tg/yr，但是沿岸沉积物主要为粗粒物质，并且为近源的非连续沉积，所以它们不是环境磁学研究的重点。宇宙尘埃供给为 0.002 Tg/yr（表 1），尽管其在冰川中是可以测量到的（Lanci et al., 2012），但是其对环境磁学研究的贡献可忽略（Itambi at al., 2010a）。火山也间歇地输入一定量的火山灰（大约 375 Tg/yr，表 1）到海洋沉积物中，火山灰层对于相关性和定年研究十分重要，但是缺乏古气候信息。

表 1. 世界海洋的总陆源输入估计表*

来源	沉积物总沉积量 (Tg/yr)	河口和沿海地区 (Tg/yr)	大陆架和大陆坡 (<1000 mwd) (Tg/yr)	深海 (>1000 mwd) (Tg/yr)
冰川(1)	2,900		1,400	1,500
河流 (2)	20,000	18,000	1,700	300
粉尘 (3)	1,100		1,000	100
沿海侵蚀 (1)	200	200	0	0
宇宙颗粒 (4)	0.002		0.0002	0.0018
火山喷发物质 (5)	375		40	335
总量	24,575		22,340	2,235

*(1) Raiswell et al.（2006）; (2) Milliman and Syviyski（1992）; (3) 经 Maher et al.（2010）报道数据计算; (4) 修改自 Love and Brownlee（1993）; (5) 经 Straub and Schmincke（1998）计算并外推至世界大洋. 按照 Raiswell et al.（2006）的方法，对不同地点陆源输入的组分进行计算。灰色区代表河口沿海地区和大陆架大陆坡地区可以被严格区分。

目前，冰川占地球表面积的不到 10%，主要位于高纬地区（＞60°）。河流几乎遍布所有纬度地区，但是其在极地区域的贡献并不重要，主要在气候温和地区、低纬地区和季风主导的陆内区域贡献较大。粉尘主要来源于低纬度大面积的内陆地区（如：亚洲）以及沙漠地区（如：撒哈拉、阿拉伯、澳大利亚、纳米比亚和阿塔卡玛），这些地区几乎没有现今河流活动（Maher et al., 2010）。由于空气和水的携载能力较低，所以分别只有 10%和 2%的粉尘和河流搬运物能到达深海沉积环境。相反，冰川却可以将 50%的沉积物负载搬运到深海沉积（表 1）。很多机制都可以改变陆源沉积物的沉积信息。首先是与地球自转或者入海口有关的底层流可以对沉积物进行再次改造，另外一个更为广泛的可以改造陆源沉积物沉积信息的过程是沉积物成岩作用，这主要是由细菌对有机质降解作用驱动的。下面我们会讨论如何根据磁学性质提取海洋沉积物中的环境信息，包括陆源沉积物的沉积信息和再次改造。

1. 冰川搬运的陆源碎屑物

由于冰川遇到水会融化，所以由冰川剥蚀并搬运到海洋中的沉积物（1400 Tg/yr，表 1）有一半聚集在大陆架和大陆坡等近源环境（Raiswell et al., 2006）。这些颗粒范围由巨砾到粘土，主要受重力流和底层流的再改造影响。另外一部分冰川剥蚀的颗粒（1500 Tg/yr）由冰山搬运到更远的地方（Raiswell et al., 2006）。当冰山融化后，这些粒径范围由粗砂到粘土的冰筏碎屑（IRD）颗粒下沉聚集在海底。IRD 层的典型特征是大量的粗沉积颗粒（通常大于 150 m），与生物成因的碳酸盐贫乏的细粒沉积物（通常为粘土）互层。IRD 层在两半球中都有存在，主要在第四纪之后的冰期，但是在 Heinrich 事件期间，Laurentide 冰架（LIS）的 IRD 层损耗到北大西洋中（Heinrich, 1988; Hemming, 2004; Stanford et al., 2011）。这些事件对应着冰川末期百年尺度的暖期，记录了大量冰川的突然卸载。由于 LIS 汇集的主要为富含（钛）磁铁矿的强磁性火山岩，所以 IRD 层的磁化率值远高于母质沉积物的磁化率（Stoner and Andrews, 1999）。因此，磁化率不仅可以作为有效指标来描述北大西洋 IRD 层的范围和厚度，而且可以用来推断它们的源区和同时期的气候模式（Robinson, 1986; Grousset at al., 1993; Dowdeswell et al., 1995; Robinson et al., 1995; Lebreiro et al., 1996）。与含量和粒径有关的磁学参数可用来进一步证实由磁化率得到的结

论，也可用来研究远到伊比利亚半岛的 IRD 范围（Robinson, 1986; Stoner et al., 1996, 1998; Thouveny et al., 2000）。但是，IRD 层不同水平层位的特殊磁学特征，以及与 HE 事件无关的 IRD 层的存在，越来越表明作为 IRD 层源区的其他冰原（如：东格陵兰岛、英国、冰岛、芬诺斯堪迪亚）的主导作用，从而也证实了之前根据 IRD 同位素信息得到的推论（Grousset et al., 2000）。根据老的北大西洋沉积物的磁学特征可以将冰筏碎屑追踪到晚始新世（Eldrett et al., 2007），这表明通过研究冰川搬运到海洋的陆源碎屑物的岩石磁学特征，可以更好地约束古气候演化。

尽管岩石磁学方法可用来识别 IRD，但是我们发现只有少量的研究利用环境磁学参数（尤其χ）来研究南极的 IRD（Huo et al., 1998; Brachfeld et al., 2002; Kanfoush et al., 2002; Pirrung et al., 2002; Venuti et al., 2011）。在整个早第三纪期间，暖池包围着南极（Ehrmann and Mackensen, 1992），这便阻碍了 IRD 在该时期的长距离搬运，但是流速的严重影响使第四纪 IRD 层的解释更为复杂（Pirrung et al., 2002）。无论如何，由于相对于母质沉积物 IRD 层具有较高的磁性矿物含量，所以和第四纪北大西洋 IRD 层类似，南极 IRD 层的主要特征是具有较高的磁化率值（Kanfoush et al., 2002; Pirrung et al., 2002; Venuti et al., 2011）。

2. 风搬运的陆源碎屑沉积物

通常，当火山和海底水热矿化（Dekov et al., 2009, 2010）对沉积物的贡献较小时，风成粉尘的磁性明显高于母质沉积物和生物成因沉积物。因此，磁化率，作为一个普遍应用的岩石磁学参数，可以用来研究不同风成粉尘的变化，如来源于沙漠（如：撒哈拉、阿拉伯、澳大利亚和巴塔哥尼亚）和内陆地区（如：亚洲）并沉积在邻近的海盆如红海（Rohling et al., 2008）、印度洋（Bloemendal and deMenocal, 1989）、太平洋（Doh et al., 1988; Yamazaki, 2009）和北大西洋（Bloemendal and deMenocal, 1989; Itambi et al., 2009, 2010a, 2010b）的粉尘。这些研究对于理解高低纬气候对季风气候演化的影响具有十分重要的贡献。但是，对磁化率数据和其他环境参数以及粉尘输入的辅助指标的综合分析表明，除了一些良好记录外（Rohling et al., 2008），由于其他陆内物源和磁性矿物的还原成岩作用的影响（Bloemendal et al., 1988, 1993; Hounslow and Maher, 1999;

Larrasoaña et al., 2008; Itambi et al., 2009），粉尘和磁化率之间的联系并不明确。前人的研究都表明，其他磁学参数，尤其是那些可以指示高矫顽力矿物相对（S-ratio）或者绝对含量（HIRM 及类似的参数）的参数，可作为风成粉尘输入的指标（图 1）（inarès-Turell et al., 2003; Larrasoaña et al., 2003a; Köhler et al., 2008; Maher, 2011; Roberts et al., 2011c）。沙漠的氧化和脱水环境使得赤铁矿大量存在于风成粉尘中，并可以利用环境磁学方法很容易地检测出来（Robinson, 1986; Doh et al., 1988; Bloemendal et al., 1988, 1993; Balsam et al., 1995; Yamazaki and Ioka, 1997b; Hounslow and Maher, 1999; Maher and Hounslow, 1999; Maher and Dennis, 2001; Dinarès-Turell et al., 2003; Larrasoaña et al., 2003a, 2008; Köhler et al., 2008; Itambi et al., 2009; Maher, 2011; Roberts et al., 2011c）。但是，需要注意的是，大部分实验室中用来使样品获得 IRM 的仪器所加外场不能超过 1T，这种情况下，针铁矿几乎不能被磁化。因此，尽管地球化学指标和 DRS 证据都指示了针铁矿的存在（Robinson, 1986; Köhler et al., 2008），但是几乎所有用来测量高矫顽力矿物含量的磁学参数都只记录了赤铁矿的含量。该情况的好处在于这些偏于赤铁矿的参数可以用来鉴别位于干热气候区域的粉尘源区（Maher, 1986）。例如，Larrasoaña et al.（2003a）利用气象学、卫星和地球化学数据识别出堆积在东部地中海的粉尘源区为撒哈拉分水岭北面的东撒哈拉地区（～21°N）。粉尘源区的精确测定使得区域性干燥度变化的研究成为可能，干燥度的变化控制着风速或者大气环流模式的变化。尽管这些参数十分重要，但在风成粉尘输入的研究中通常忽略了这些参数的分离。
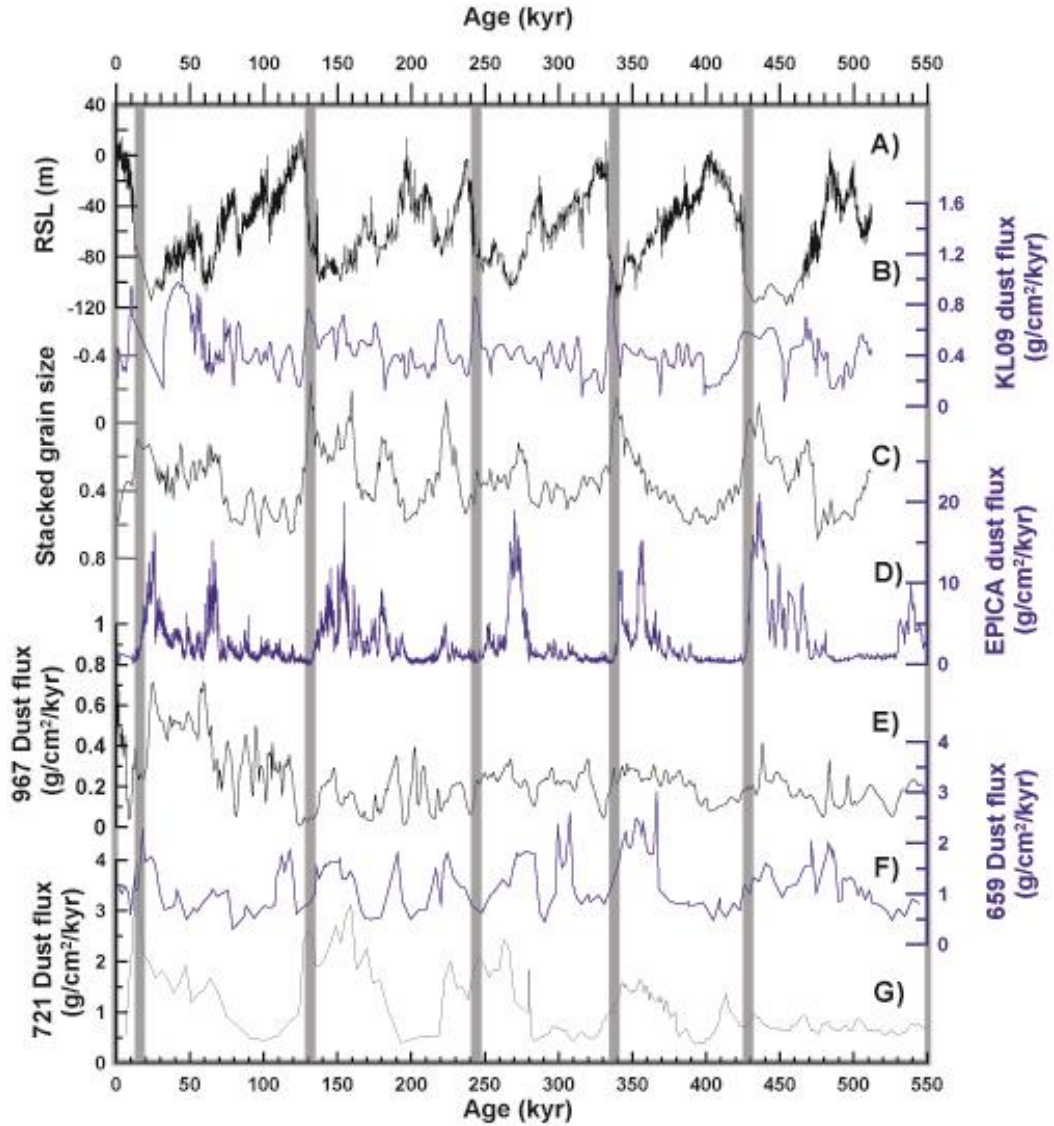
图 1. 红海和南极洲、北非的海平面和粉尘记录对比（参考 Roberts et al.（2011c））. 垂直
灰色条带代表了 5 个冰期转换位置. (A) 海平面（Rohling et al., 2009）；(B) 红海 KL09 孔
的粉尘记录（Roberts et al., 2011c）；(C) 中国黄土高原赵家川和灵台剖面的粒径信息（Sun
et al., 2006b）；(D)-(G)分别为南极洲EPICA Dome C 的粉尘记录（Lambert et al., 2008），ODP
967 孔的粉尘记录（Larrasoaña et al., 2003a）, 659 孔的粉尘记录（Tiedemann et al., 1994），
721 孔的粉尘记录（deMenocal et al., 1991）。

3. 河流搬运的陆源碎屑沉积物

尽管河流是海洋沉积物的主要供给，但是海洋沉积物中的河流成因沉积物
并不是环境磁学的研究重点。这可能是因为河流搬运到海洋中的沉积物主要受
自动循环（如：河道转位）和变周期（如：潮汐和潮退控制的便利空间）的因

素控制，而不是气候因素。所以，有一些研究磁化率应用的例证认为随着碎屑颗粒含量或者粒径的增加，磁化率增加是由于陆源供给增加引起的（Weber et al., 2003; Stein et al., 2004; Alt-Epping et al., 2009; De Vleeschouwer et al., 2011），而这些陆源供给的主要动力学机制为从季风到高纬度控制的沉积，或者二者相互作用（Weber et al., 2003）。尽管在海面上升时期，陆源碎屑物质主要保存在三角洲地区，与气候控制的河流供给相比，这是主要的沉积记录，但是结合其他与含量和粒径有关的磁学参数推断，这可能是陆源供给或者源区的变化，比如亚马逊河（Maslin et al., 2000）和恒河-雅鲁藏布江（Prakash Babu et al., 2010）。在其他情况下，河流成因的海洋沉积物中记录的气候信息与河流的卸载无关，而是与源区干燥度变化有关（Zhang et al., 2007）。所以，在顺风的热带河流中，赤铁矿/针铁矿比值与源区干燥度的变化有关，因为与针铁矿相比，赤铁矿形成于更干燥的环境中（Maher, 1986）。Abrajevitch et al.（2009）利用岩石磁学方法得到这两种矿物的比值，以此来推断季风控制的恒河-雅鲁藏布江的河流卸载的周期性变化。另外，Colin et al.（1998）也提出恒河-雅鲁藏布江和伊洛瓦底江源区的干燥度变化限制着这些河流搬运的磁铁矿的含量及粒径。

4. 底层流对沉积物的再次改造

海洋沉积物一旦沉积，底层流便会对其进行改造，影响其初始的物理特征和沉积信息。这会导致所谓的等深流积层或者漂流沉积，其特征和分布与纬度无关（Faugeres and Stow, 1993）。尽管底层流的活动与气候变化之间的联系并不是完全清楚（Andrews et al., 2003a, b; Rousse et al., 2006），但是第四纪漂流沉积物中与含量和粒径有关的磁学参数可用来检测底层流的强度变化，主要是北大西洋（Kissel et al., 1997, 1998, 1999, 2009; Andrews et al., 2003a, 2003b; Hassold et al., 2006; Rousse et al., 2006; Stanford et al., 2006]和南极洲周围（Mazaud et al., 2007, 2010）。底层流不仅影响漂流沉积物中粒径的分选，并且也会影响颗粒的空间分布。这会引起初始沉积物组构的增强，根据沉积物磁组构（磁化率各向异性，AMS）的方向性质（Parés et al., 2007）以及各向异性的形状和角度（Kissel et al., 1997, 1998; Hassold et al., 2006, 2009a, b）可以推断出底层流的动力学机制。大部分关于漂流沉积物的岩石磁学和 AMS 研究重点研究了高纬度如北大西洋和环南极洲盆地等地区的底层流动力机制。

5. 混合陆源沉积物信息

尽管在一些特定的纬度地区，海洋陆源碎屑沉积物是由不同的源区控制，但是在这些纬度之间的区域陆源碎屑沉积却是混合信息。在低纬度的东北大西洋（图2）（Bloemendal et al., 1988; Itambi et al., 2009, 2010b; Just et al., 2012）和南中国海（Kissel et al., 2003）的海洋沉积记录中就发现了风成粉尘和河流搬运的混合陆源沉积物。总之，这些研究中提出了粉尘和河流供给的反相关关系。一个研究混合陆源信息的典型例子是从伊比利亚半岛搬运形成的IRD层中识别出来自撒哈拉沙漠的风成赤铁矿（Robinson, 1986; Thouveny et al., 2000）。富含风成物质和IRD的沉积物通常综合了高低纬的背景信息。不同陆源源区的沉积物共存表明气候变化可以改变这些物质的纬度分布。与南极冰芯粉尘沉积物的地球化学记录一致，根据环南极洲海洋沉积物的磁化率记录可以推断出风成粉尘和IRD记录的混合信息（Pugh et al., 2009）。这表明磁化率记录与粉尘供给有关，不论是来自巴塔哥尼亚还是澳大利亚的粉尘（Grousset et al., 1992; De Deckker et al., 2010）。这是十分重要的，因为海洋沉积物和冰芯记录之间的联系可以为那些很难确定年龄的沉积物建立详细的年龄模型（Pugh et al., 2009）。但是，其他研究则将环南极洲的海洋沉积物的磁化率记录作为IRD的信息（Huo et al., 1998; Kanfoush et al., 2002; Pirrung et al., 2002）。另外，南极绕极流对环南极海洋沉积物的再改造使得IRD和粉尘的信息更为复杂（Parés et al., 2007; Mazaud et al., 2007, 2010; Hassold et al., 2009a, b）。在西北太平洋存在同样的复杂情况，IRD和风成粉尘，还有火山灰共同影响沉积物的磁学性质（Bailey et al., 2011）。
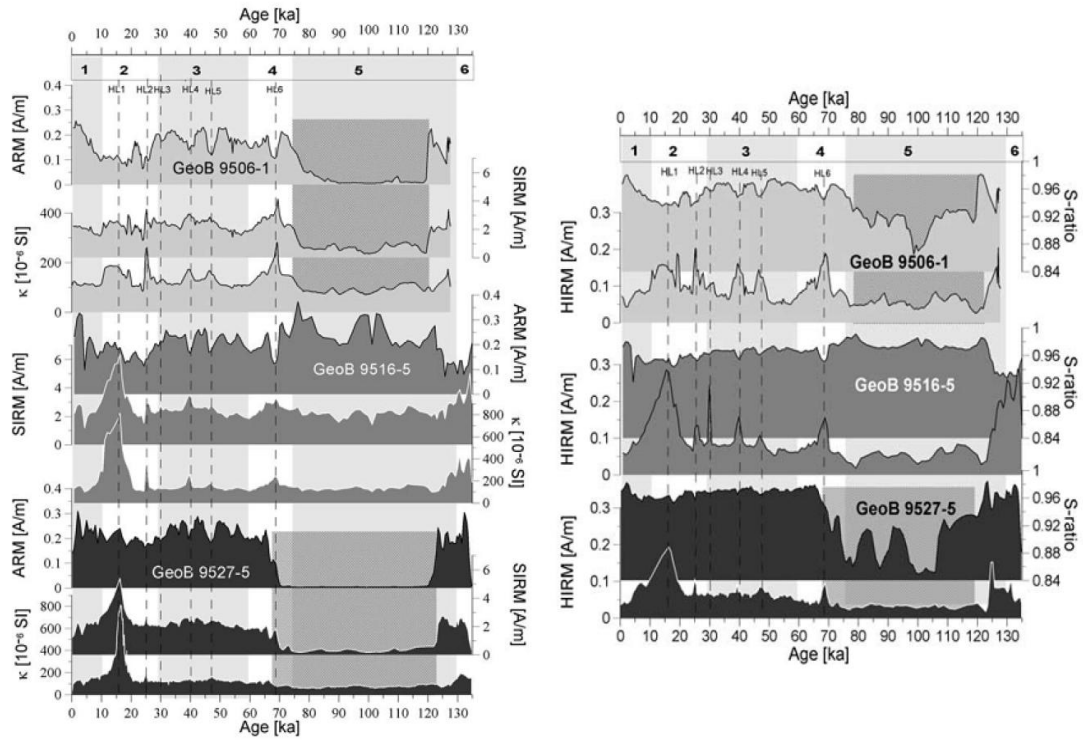
图2. 海洋沉积钻孔 GeoB 9506-1、GeoB 9516-5 和 GeoB 9527-5 的磁学参数-年代曲线（Itambi et al., 2009）。暖期较高的 S-ratio 值（水平标尺指示了氧同位素的 1 到 6 阶）表明主要的载磁矿物为河流相磁铁矿，但是其含量（根据 ARM 曲线）在 HL1-HL6 期间气候变得冷干时减小。但是在 HL1-HL6 期间，HIRM 和 κ 的增加以及较低的 S-ratio 值表明，富含赤铁矿的撒哈拉沙漠粉尘输入增加。由于陆源沉积中的河流和风搬运主要受纬度控制，所以 ARM 和 HIRM 分别在最南和最北端的钻孔中达到最大值，钻孔 GeoB 9506-1 和 GeoB 9527-5 在 70-120 ka 间，HIRM 缓慢降低，ARM 和 S-ratio 明显降低证明在 MIS 5 期间，磁铁矿大量溶解，而赤铁矿只是部分溶解。很明显，不同的参数反映了不同的古气候过程。

文献速递

1. 南大洋冰期时形成的绕极地风带

翻译人：仲义 zhongy@sustech.edu.cn

摘要：通过风尘作用将溶解 Fe 的带入贫铁的南大洋可以导致初级生产力和碳输出，进而使得冰期大气 CO_2 的降低。然而，在末次冰期对于南大洋风尘的来源和路径仍然未知。研究表明，南美中部（～24-32 °S）在末次冰期通过环南极风尘搬运贡献了南太平洋亚南极区域～80%的风尘通量，而南极区域的风尘堆积主要来自于澳洲。这一模式与现今及全新世模式相反，南太平洋风尘通量被认为主要来源于澳洲大陆的来源。我们结果显示在南大洋冰期，铁的施肥效应主要依赖于南美中部沙尘铁源变化与环极西风系统的动态相互作用。

ABSTRACT: The increased flux of soluble iron (Fe) to the Fe-deficient Southern Ocean by atmospheric dust is considered to have stimulated the net primary production and carbon export, thus promoting atmospheric CO_2 drawdown during glacial periods. Yet, little is known about the sources and transport pathways of Southern Hemisphere dust during the Last Glacial Maximum (LGM). Here we show that Central South America (~ 24–32 °S) contributed up to ~ 80% of the dust deposition in the South Pacific Subantarctic Zone via efficient circum-Antarctic dust transport during the LGM, whereas the Antarctic Zone was dominated by dust from Australia. This pattern is in contrast to the modern/Holocene pattern, when South Pacific dust fluxes are thought to be primarily supported by Australian sources. Our findings reveal that in the glacial Southern Ocean, Fe fertilization critically relies on the dynamic interaction of changes in dust-Fe sources in Central South America with the circumpolar westerly wind system.

Figure 1. Sample locations in the South Pacific. Main terrestrial potential source areas (PSAs) indicated with white labels. South American dust sources are grouped into latitudinal bands. In the text, PSAs between 24 and 32 °S are also referred to as Central South America, whereas Southern South America describes the PSAs south of 32 °S. Southern Ocean fronts from ref. 94. STF: Subtropical Front. SAF: Subantarctic Front. APF: Antarctic Polar Front. SACC: Southern ACC Front. SAZ: Subantarctic Zone. PFZ: Polar Frontal Zone. AZ: Antarctic Zone. Map created with Ocean Data View95.

Figure 2. The transport and deposition of dust in the South Pacific during the Last Glacial Maximum. a

The distribution of dust fraction [206]Pb/[204]Pb in the glacial South Pacific. Solid and dashed white lines delineate the limits of 40% and 15% winter sea-ice cover during the Last Glacial Maximum (LGM)[77], respectively. Black dots: LGM time slice sampling locations. The dashed black outline indicates the modern zones of increased wintertime wind speed maxima in the high-altitude (200 hPa) westerly wind flow of the subtropical (STJ) and subpolar (SPJ) branches of the jet stream located north and south of the reduced mid-latitude jet (MLJ), respectively[73]. Terrestrial source data from the literature listed in Supplementary Table 3. It is noteworthy that some original terrestrial sample coordinates were slightly modified to improve visibility in this figure. Ocean fronts from ref. [94]. STF: Subtropical Front. SAF: Subantarctic Front. APF: Antarctic Polar Front. SACC: Southern ACC Front. SAZ: Subantarctic Zone. PFZ: Polar Frontal Zone. AZ: Antarctic Zone. Map created with Ocean Data View software[95]. b The LGM wintertime scenario. The northward expanded Southern Hemisphere westerly wind (SWW) system (STJ present in the South Pacific as in a) delivers dust efficiently on a circumpolar trajectory from Central South America to the study area. The extensive sea-ice cover reduces the dust deposition in the South Pacific AZ. IRD: ice-rafted detritus. Numbers in yellow box as in a. c The LGM summertime scenario. The STJ transporting dust from Central South America is absent, the SWW move closer to Antarctica and deliver predominantly Australian dust to the South Pacific AZ and SAZ north of the summer sea-ice limit. Numbers in green box as in a. A comprehensive overview of tracer evidence constraining our proposed LGM scenario of circumpolar dust transport and deposition in the study area is provided in Supplementary Table 4.

2. 海洋碳循环扰动驱动二叠纪-三叠纪生物大灭绝

翻译人：蒋晓东 **jiangxd@sustech.edu.cn**

摘要：大约 251.9 Ma 的地质记录中二叠纪-三叠纪边界呈现出显著的环境危机，这推动了生命向前演化。西伯利亚的岩浆作用被认为发挥了重要作用，但其触发机制和反馈机制并未被充分的理解。本研究对特提斯陆架腕足类壳体进行 B 同位素（海水 pH）分析，结果表明海水 pH 降低同步于二叠纪末生物大灭绝。再结合碳同位素数据，本研究建立了地球化学模型，用于解决碳循环动力学以及海洋氧化还原和氮同位素的转变。研究发现初始的海洋酸化与西伯利亚岩浆作用的大规模碳排气密切相关。本研究揭示了温室效应对海洋环境的影响，揭示上升的海表温度，增强的化学风化引起营养输入和生产力升高，进一步引起三叠纪初期广泛的大洋脱氧和零星的硫化物中毒。该发现使我们能够利用地球化学数据重建这一引起显生宙生物大灭绝的机制。

ABSTRACT: The Permian/Triassic boundary approximately 251.9 million years ago marked the most severe environmental crisis identified in the geological record, which dictated the onwards course for the evolution of life. Magmatism from Siberian Traps is thought to have played an important role, but the causational trigger and its feedbacks are yet to be fully understood. Here we present a new boron-isotope-derived seawater pH record from fossil brachiopod shells deposited on the Tethys shelf that demonstrates a substantial decline in seawater pH coeval with the onset of the mass extinction in the latest Permian. Combined with carbon isotope data, our results are integrated in a geochemical model that resolves the carbon cycle dynamics as well as the ocean redox conditions and nitrogen isotope turnover. We find that the initial ocean acidification was intimately linked to a large pulse of carbon degassing from the Siberian sill intrusions. We unravel the consequences of the greenhouse effect on the marine environment, and

show how elevated sea surface temperatures, export production and nutrient input driven by increased rates of chemical weathering gave rise to widespread deoxygenation and sporadic sulfide poisoning of the oceans in the earliest Triassic. Our findings enable us to assemble a consistent biogeochemical reconstruction of the mechanisms that resulted in the largest Phanerozoic mass extinction.
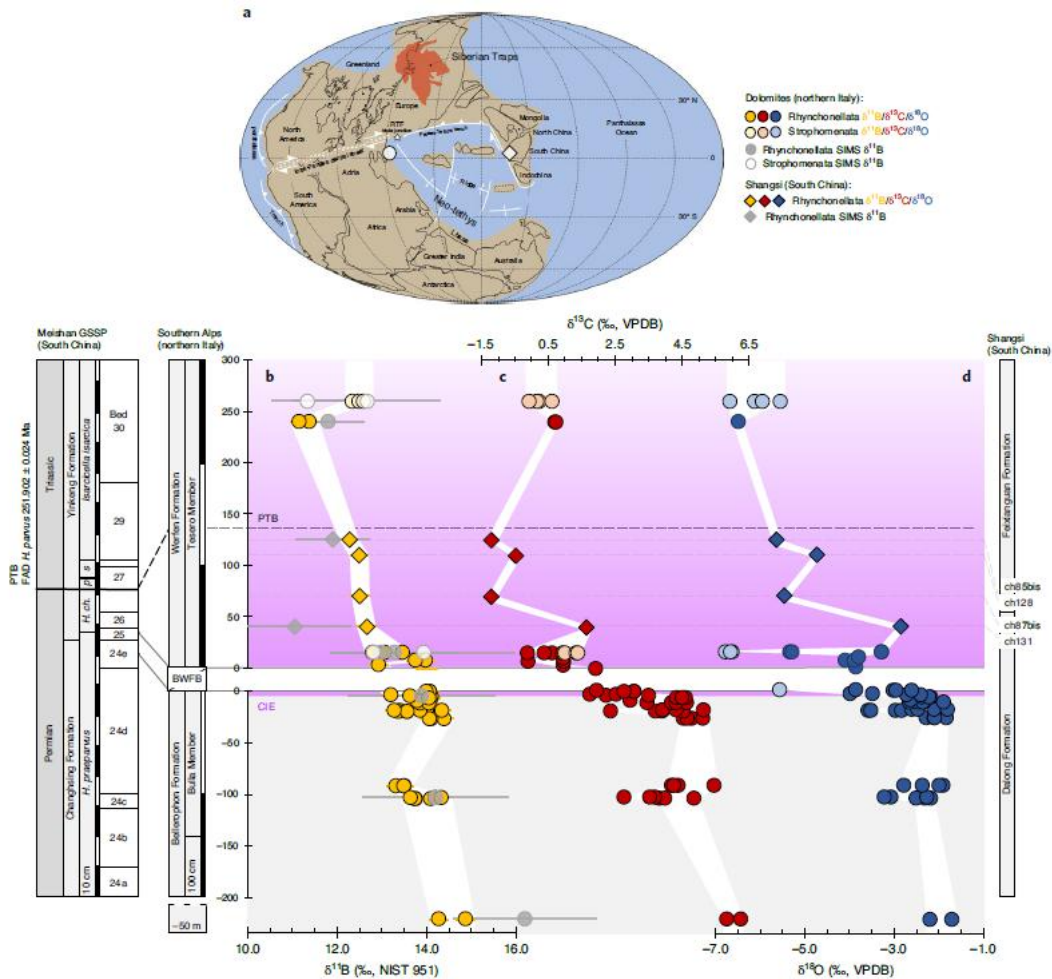
Figure 1. Brachiopod-based stable isotope data from Italy and China. a, Late Permian palaeogeographic reconstruction (Methods) with the locations of the sampling sites. b–d, $\delta^{11}B$ (b), $\delta^{13}C$ (c) and $\delta^{18}O$ (d) records derived from brachiopod shells from Southern Alps (Sass de Putia, Tesero and Val Brutta) and South China (Shangsi). The error bars in b indicate the analytical uncertainty for solution-based $\delta^{11}B$ (2 s.d. = 0.2‰) and the s.d. between multiple ion spots measurements within a single shell for SIMS $\delta^{11}B$. The stratigraphy of the Meishan Global Boundary Stratotype Section and Point (GSSP) is shown for comparison. The purple field marks the onset of the CIE as defined in our age model (Methods and

Supplementary Information), with the geochronology based on the latest age estimates1. Conodont zones: Hindeodus praeparvus, H. changxingensis, H. parvus, Isarcicella staeschei and I. isarcica. BWFB, Bellerophon– Werfen Formation boundary; FAD, first appearance datum; Ma, million years ago; NIST, National Institute of Standards and Technology; VPDB, Vienna Pee Dee Belemnite; RTF, ridge trench fault.

3. 里奥格兰德裂谷之下活跃的地壳分异作用

翻译人：冯婉仪 fengwy@sustech.edu.cn

摘要：富硅的大陆地壳是地球所特有的。在高温-超高温变质过程（700 ℃至> 900 ℃）期间发生的部分熔融提高了地壳的长期稳定性，这是因为它重新分配了地壳和地幔之间的关键元素，并且最终产生更冷、更演化的大陆。麻粒岩（形成于高温-超高温条件下的岩石）保存了地球大陆稳定性的记录，但驱动麻粒岩形成的构造机制却神秘莫测。在这里，我们分析了来自里奥格兰德裂谷的下地壳捕虏体，这个裂谷是美国西南部一个新生的伸展带。铀-铅地质和热年表结合热气压模拟表明，地壳下部 10 公里处目前处于麻粒岩相的条件，最下部的2 公里处处于超高温的条件。地壳和地幔捕虏体定义了一个连续的压力和温度序列，表明一个薄的岩石圈地幔盖可以将升高的传导热传递到地壳。这些发现建立了超高温变质作用、Laramide 造山带垮塌和岩石圈地幔减薄之间的直接联系。现今超高温变质作用的其他指标与普遍存在于美国-墨西哥盆地和山脉省数千平方公里的这些条件一致。里奥格兰德下地壳的压力-温度路径与出露的麻粒岩地质体的压力-温度路径的相似之处表明，增厚之后岩石圈的伸展是导致大陆地壳分异的主要机制。

ABSTRACT: Silicon-rich continental crust is unique to Earth. Partial melting during high- to ultrahigh-temperature metamorphism (700 °C to > 900 °C) promotes the long-term stability of this crust because it redistributes key elements between the crust and mantle and ultimately produces cooler, more-differentiated continents. Granulites—rocks formerly at high- to ultrahigh-temperature conditions—preserve a record of the stabilization of Earth's continents, but the tectonic mechanisms that drive granulite formation are enigmatic. Here we present an analysis of lower-crustal xenoliths from the Rio Grande Rift—a nascent zone of extension in the southwestern United States. Uranium–lead geo- and thermochronology combined with

thermobarometric modelling show that the lower 10 km of the crust currently resides at granulite-facies conditions, with the lowermost 2 km at ultrahigh-temperature conditions. Crust and mantle xenoliths define a continuous pressure-and-temperature array, indicating that a thin lithospheric mantle lid mediates elevated conductive heat transfer into the crust. These findings establish a direct link among ultrahigh-temperature metamorphism, collapse of the Laramide orogen and lithospheric mantle attenuation. Other indicators of modern ultrahigh-temperature metamorphism are consistent with these conditions prevailing over thousands of square kilometres across the US–Mexico Basin and Range province. Similarities between the pressure-and-temperature path from the Rio Grande lower crust and those from exhumed granulite terranes imply that post-thickening lithospheric extension is a primary mechanism to differentiate Earth's continental crust.
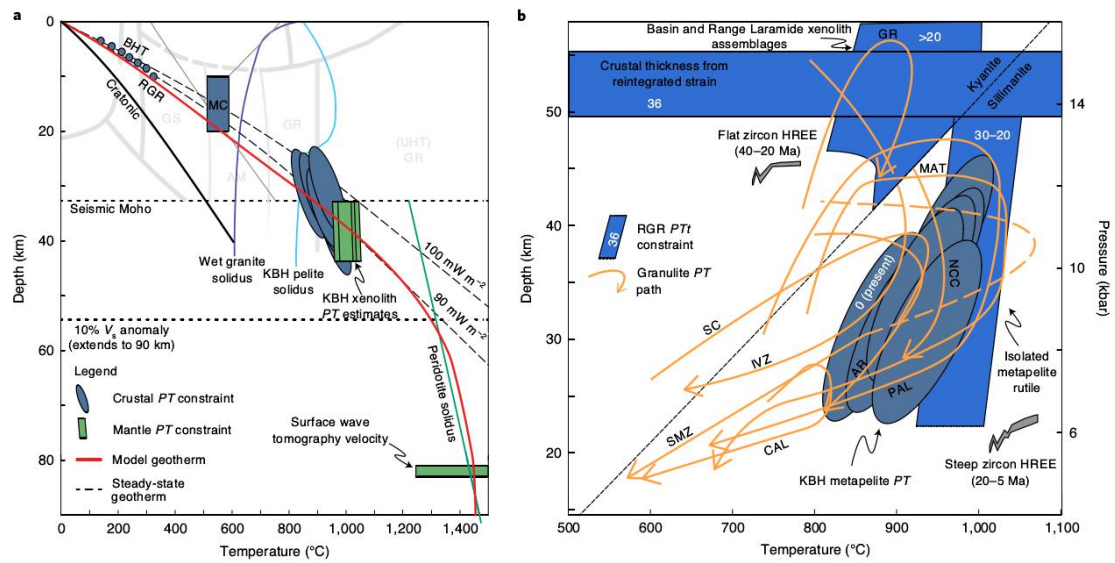
Figure 1. Modern-day lithospheric geotherm beneath KBH and comparison with ancient granulite terranes. a, Temperature-depth constraints are from metapelite thermobarometry (blue ellipses), depth to the magnetite Curie isotherm (MC; blue rectangle) and extrapolation from near-surface measurements (BHT; blue circles). Mantle depth and temperature estimates (green rectangles) are from two-pyroxene thermometry and the seismically defined Moho beneath KBH[17], as well as temperature inversions from surface wave tomography velocities[52]. Also shown are the dry peridotite solidus[53], 0.4 °C km^{-1} mantle adiabat, wet granite solidus[54], metamorphic facies grid and aluminosilicate phase diagram. Steady-state geotherms calculated for the observed range of surface heat flows near KBH are

16

shown as black dashed lines; the solid red line represents model geotherm calculated for 30 Myr of depth-dependent thinning (crustal and mantle thinning factors: 1.25 and 6, respectively) and the black line represents stable cratonic geotherm using adjacent Great Plains surface heat flow and crustal thickness[55]. b, Comparison of RGR PTt constraints with PT paths derived from exhumed granulite terranes (orange arrows; see Supplementary Information for full reference list). Light-blue polygons represent > 20 Ma PT constraints from the RGR (ages are superimposed); darker ellipses correspond to modern PT constraints. Zircon REE patterns (embedded) from KBH mafic granulites show evolution from garnet-present to garnet-absent conditions. Also shown is the aluminosilicate phase diagram. IVZ, Ivrea Zone, Italy; MAT, Rauer Group, East Antarctica; PAL, Palni Hills, south India; SMZ, Southern Marginal Zone, Limpopo Complex, South Africa; GR, central Grenville; AR, Arunta Complex, central Australia; CAL, southern Calabria, Italy; NCC, North China Craton.

4. Tamu Massif 磁异常揭示出海底扩张引起海底高原的形成

翻译人：李园洁 liyj3@sustech.edu.cn

摘要：Tamu Massif 是一个巨大的中生代海底火山，是 Shatsky Rise 海底高原的主要火山机构。它位于一个扩张脊三联点，但是被认为是出露地幔柱的溢流火山活动而形成的盾状火山。但是，Tamu Massif 喷发如何与具有很多线状火山的扩张脊相互作用仍不清楚。本文中作者制出 Tamu Massif 的磁异常图，可提供地壳形成的线索。对于 Tamu Massif，作者发现线性的磁异常主要是相反极性的洋壳形成的。这种模式表明 Tamu Massif 不是盾状火山而是大量的脊上火山侵位形成的。如果 Shatsky Rise 的地幔源是地幔柱，那么它与海底扩张相关并由其控制。由于这个因素，即使最大的海底高原火山机构也是由海底扩张形成的。作者建议目前广泛接受的大陆溢流玄武岩与海底高原可类比的观点需要重新考虑。

ABSTRACT：Tamu Massif is an immense Mesozoic submarine volcano, the main edifice of the Shatsky Rise oceanic plateau. It is located at a spreading ridge triple junction, but considered to be a shield volcano formed by effusive volcanism from an emerging mantle plume. However, it is unclear how Tamu Massif eruptions interacted with the spreading ridges, which are enormous linear volcanoes themselves. Here we create a magnetic anomaly map for Tamu Massif, which can provide clues about crustal formation. For Tamu Massif, we find dominantly linear magnetic field anomalies caused by crustal blocks of opposite magnetic polarity. This pattern suggests that Tamu Massif is not a shield volcano, but was emplaced by voluminous, focused ridge volcanism. If the magma source at the Shatsky Rise was a plume, it was closely connected to and controlled by seafloor spreading. By implication, even the largest oceanic plateau edifices can be formed by seafloor spreading. We suggest that the widely accepted analogy between continental flood basalts

and oceanic plateaus requires reconsideration.
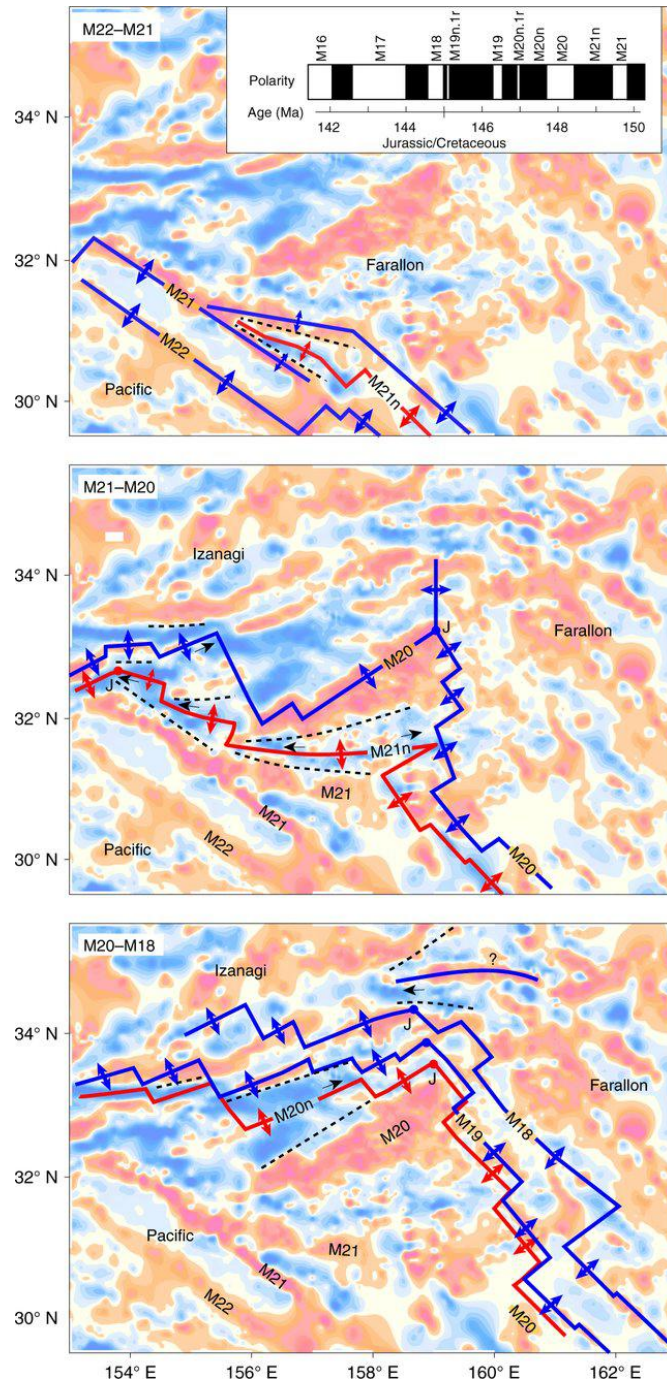
Figure 1. Reconstruction of magnetic anomaly formation within Tamu Massif. Top, the formation of the split M21 anomaly by ridge propagation during Chron M21n. Inset, Late Jurassic-Early Cretaceous geomagnetic polarity timescale. Middle, the rotation of a ridge segment during M21n and M20. Bottom, the formation of magnetic anomaly bights M19-M18 on the north flank of Tamu Massif. Blue (red) lines represent negative (positive) magnetization isochrons. Double-ended arrows denote spreading

19

directions. Dashed lines enclose wedge-shaped anomalies that may indicate ridge propagation, with the direction of propagation shown by small black arrows. Red and blue dots (labeled J) show the positions of triple junctions. See Supplementary Fig. 9 for further explanation.
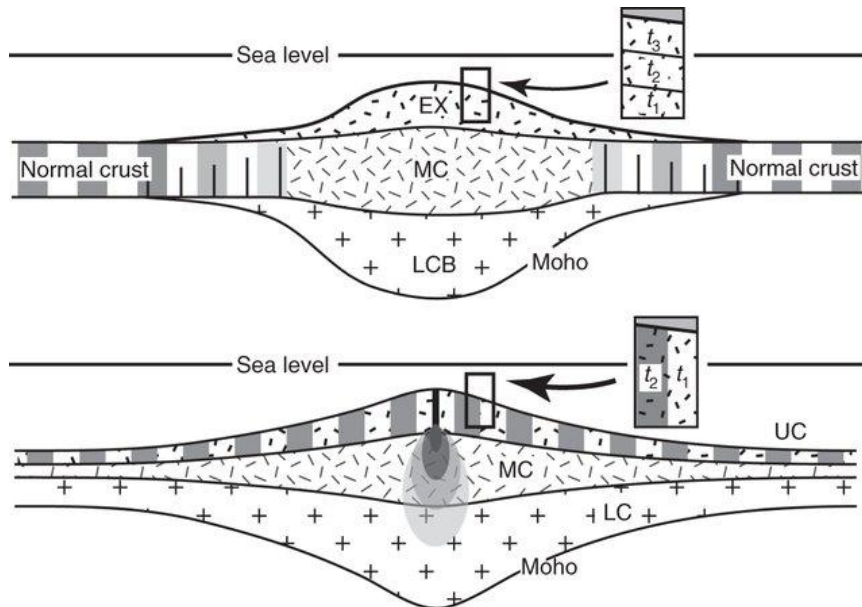
Figure 2. Schematics of an existing volcanic pulse model and a spreading model for the formation of Tamu Massif. Top, the pulse model3,10 implies the formation of a massive volcano with an extrusive top (EX) and intrusive lower crustal body (LCB) sandwiching middle crust (MC) and normal crust. Grey and white blocks in the crust indicate normal and reversedpolarity magnetization blocks. Short vertical lines represent intrusions that modify pre-existing crust. Bottom, in the spreading model, crust forms continuously with no boundary between the plateau and adjacent crust. Lateral topographic variation is caused by changes in crustal thickness, with a maximum at the centre of Tamu Massif. As above, grey and white blocks indicate magnetic polarity. UC, upper crust; LC, lower crust. The insets show the inferred volcanic succession (t_n is age, with $t_3 < t_2 < t_1$).

5. 胶黄铁矿（Fe₃S₄）具有热力学稳定性：其在地球和行星中出现的意义

翻译人：柳加波 Liujb@sustech.edu.cn

摘要：铁硫化物广泛存在于地球上，也可能存在于太阳系内外的行星中。基于生成三种磁性硫化铁相（粗相、纳米相尖晶石和高压单斜晶相胶黄铁矿（Fe₃S₄））的实测焓，我们证明在常温下胶黄铁矿是 Fe–S 相图中的稳定相。胶黄铁矿的热力学稳定性和低表面能表明细颗粒的 Fe₃S₄ 广泛存在于很多缺氧的陆地环境中。由尖晶石形成的低于 3 GPa 的热力学亚稳态的高压单斜相显示出负 P-T 斜率。这三个相的稳定性表明它们可能存在于水星上，并且可能记录了水星磁场。

ABSTRACT: Iron sulfide minerals are widespread on Earth and likely in planetary bodies in and beyond our solar system. Using measured enthalpies of formation for three magnetic iron sulfide phases: bulk and nanophase Fe₃S₄ spinel (greigite), and its high-pressure monoclinic phase, we show that greigite is a stable phase in the Fe–S phase diagram at ambient temperature. The thermodynamic stability and low surface energy of greigite supports the common occurrence of fine-grained Fe₃S₄ in many anoxic terrestrial settings. The high-pressure monoclinic phase, thermodynamically metastable below about 3 GPa, shows a calculated negative P-T slope for its formation from the spinel. The stability of these three phases suggests their potential existence on Mercury and their magnetism may contribute to its present magnetic field.
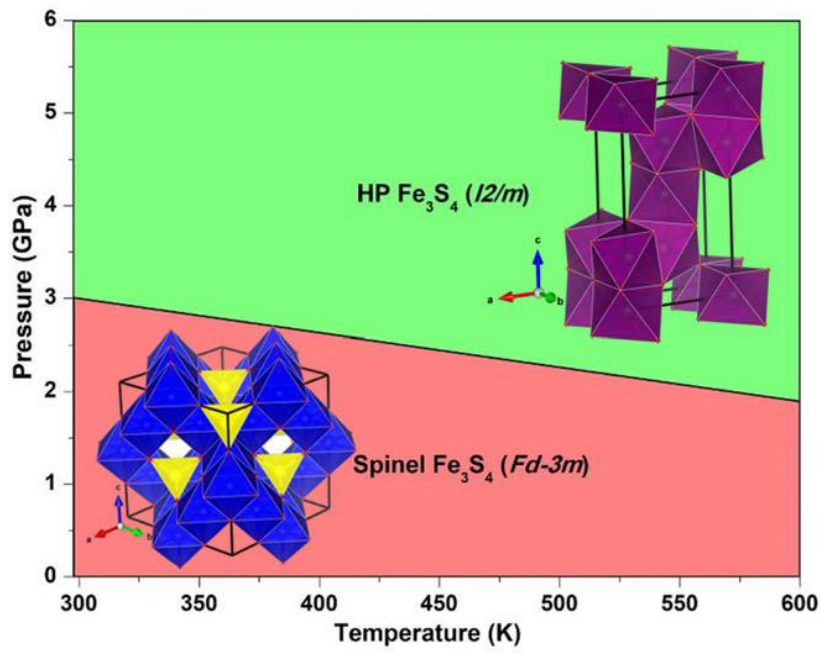
Figure 1. Calculated P-T diagram of Fe$_3$S$_4$ showing negative slope.

6. 巨型大陆在超大陆循环中的作用

翻译人：周洋 zhouy3@sustech.edu.cn

摘要：在超大陆 Pangea 之前，存在着 Gondwana 大陆，这是一个面积大约相当于 Pangea 大陆一半的"巨型大陆"。关于 Gondwana 大陆组合对 Pangea 超大陆循环起着怎样的作用，存在着许多争论。在这里，我们证明了在过去的三个超大陆循环周期中，每个周期之前约 200m.y 有类似于 Gondwana 巨型大陆的拼合，并且巨型大陆建造是超大陆聚集的地球动力学先兆。最近的欧亚大陆被认为是第四个巨型大陆，与未来的 Amasia 超大陆密切相关。我们使用来自欧亚大陆深部地幔地震学和 Gondwana 古地理学的约束条件来建立巨型大陆组合和后续超大陆聚集的动力学模型。当超大陆裂解时，一个巨型大陆沿着环绕它的俯冲带组合，在特定的位置，下沉强度是最大的。然后，巨型大陆沿着俯冲带汇聚，与其它大陆碰撞形成超大陆。 该模型的几何学特征与从 Rodinia 到 Gondwana 到 Pangea 的运动学转变是一致的。

ABSTRACT: Supercontinent Pangea was preceded by the formation of Gondwana, a "megacontinent" about half the size of Pangea. There is much debate, however, over what role the assembly of the precursor megacontinent played in the Pangean supercontinent cycle. Here we demonstrate that the past three cycles of supercontinent amalgamation were each preceded by ~ 200 m.y. by the assembly of a megacontinent akin to Gondwana, and that the building of a megacontinent is a geodynamically important precursor to supercontinent amalgamation. The recent assembly of Eurasia is considered as a fourth megacontinent associated with future supercontinent Amasia. We use constraints from seismology of the deep mantle for Eurasia and paleogeography for Gondwana to develop a geodynamic model for megacontinent assembly and subsequent supercontinent amalgamation. As a supercontinent breaks up, a megacontinent

assembles along the subduction girdle that encircled it, at a specifc location where the downwelling is most intense. The megacontinent then migrates along the girdle where it collides with other continents to form a supercontinent. The geometry of this model is consistent with the kinematic transitions from Rodinia to Gondwana to Pangea.
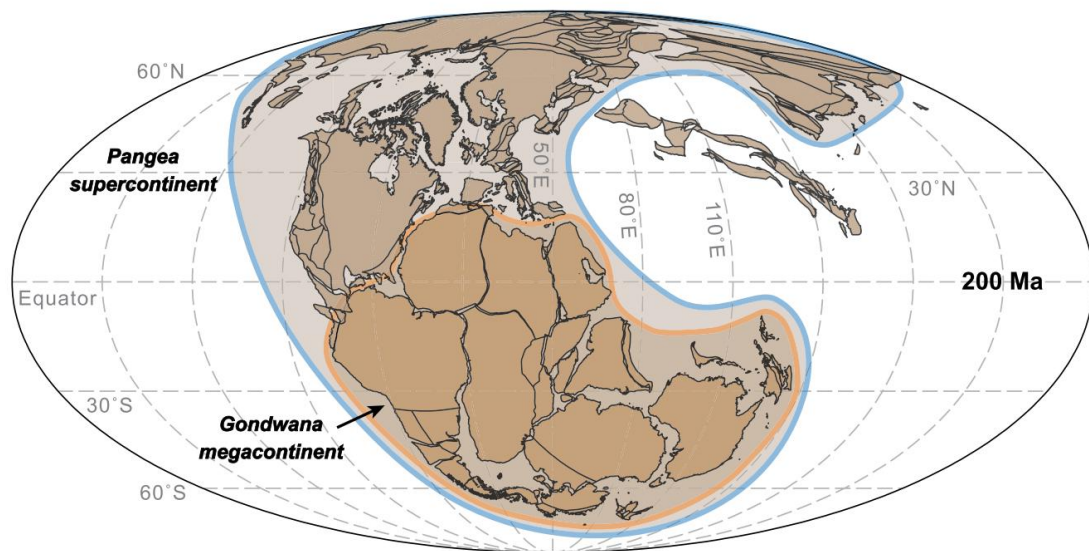
Figure 1. Paleogeographic reconstruction of Pangea before breakup, showing Gondwana megacontinent (orange) in Pangea supercontinent (blue) (Mitchell et al., 2012; Mitchell et al., 2020).

7. 古南海板块在哪里?从全球地幔对流模拟看东南亚板块构造与地幔流动历史

翻译人：刘伟 inewway@163.com

摘要：东南亚自新生代以来的"古南海"模型及其周边构造历史一直存在争议。我们将四种不同的古南海重建模型置到全球地球动力学模型中，以约束古南海板块构造和可能的板块位置。我们的板块重建考虑以下几点：向南俯冲与双向俯冲模式；早始新世或晚渐新世开始的婆罗洲逆时针旋转；以及更大或更小的菲律宾海板块重建尺寸。考虑到矿物效应和地震层析成像的有限分辨率，我们将模拟结果与层析成像结果进行了比较。所有的地球动力学模型都再现了马来西亚半岛、苏门答腊和爪哇下的层析成像冀他板块。向南的古南海俯冲产生了现在巴拉望、北婆罗洲和近海巴拉望之下的板块。古南海双向俯冲结合早期婆罗洲旋转，在南海南部 400 - 700 km 深度下产生了近水平的板片；这些模型最适合地震层析成像。一个较小的菲律宾海板块搭配一个~ 1000 公里长的琉球板片比一个大的菲律宾海板块更好。综合考虑，我们的四端元板块重建预测了古南海板块位于现在的婆罗洲、南海、苏禄和西里伯斯海以及南菲律宾板块之下的< 900 公里深处。不考虑板块重建，我们预测：中新生代印支半岛之下的被动回退上涌地幔流和晚新生代南海之下的下降地幔流不支持深部起源的海南地幔柱模型。

ABSTRACT: The plate tectonic history of the hypothesized "proto-South China Sea" (PSCS) ocean basin and surrounding SE Asia since Cenozoic times is controversial. We implement four diverse proto-South China Sea plate reconstructions into global geodynamic models to constrain PSCS plate tectonics and possible slab locations. Our plate reconstructions consider the following: southward versus double-sided PSCS subduction models; earlier (Eocene) or later (late Oligocene) initiation of Borneo counterclockwise rotations; and larger or smaller reconstructed Philippine Sea plate sizes. We compare our modeling results against tomographic images by accounting for

mineralogical effects and the finite resolution of seismic tomography. All geodynamic models reproduce the tomographically imaged Sunda slabs beneath Peninsular Malaysia, Sumatra, and Java. Southward PSCS subduction produces slabs beneath present Palawan, northern Borneo, and offshore Palawan. Double-sided PSCS subduction combined with earlier Borneo rotations uniquely reproduces subhorizontal slabs under the southern South China Sea (SCS) at ~ 400 to 700 km depths; these models best fit seismic tomography. A smaller Philippine Sea (PS) plate with a ~ 1,000-km-long restored Ryukyu slab was superior to a very large PS plate. Considered together, our four end-member plate reconstructions predict that the PSCS slabs are now at <900 km depths under present-day Borneo, the SCS, the Sulu and Celebes seas, and the southern Philippines. Regardless of plate reconstruction, we predict (1) mid-Cenozoic passive return-flow upwellings under Indochina; and (2) late Cenozoic downwellings under the SCS that do not support a deep-origin "Hainan plume." Modeled Sundaland dynamic topography strongly depends on the imposed plate reconstructions, varying by almost 1 km.
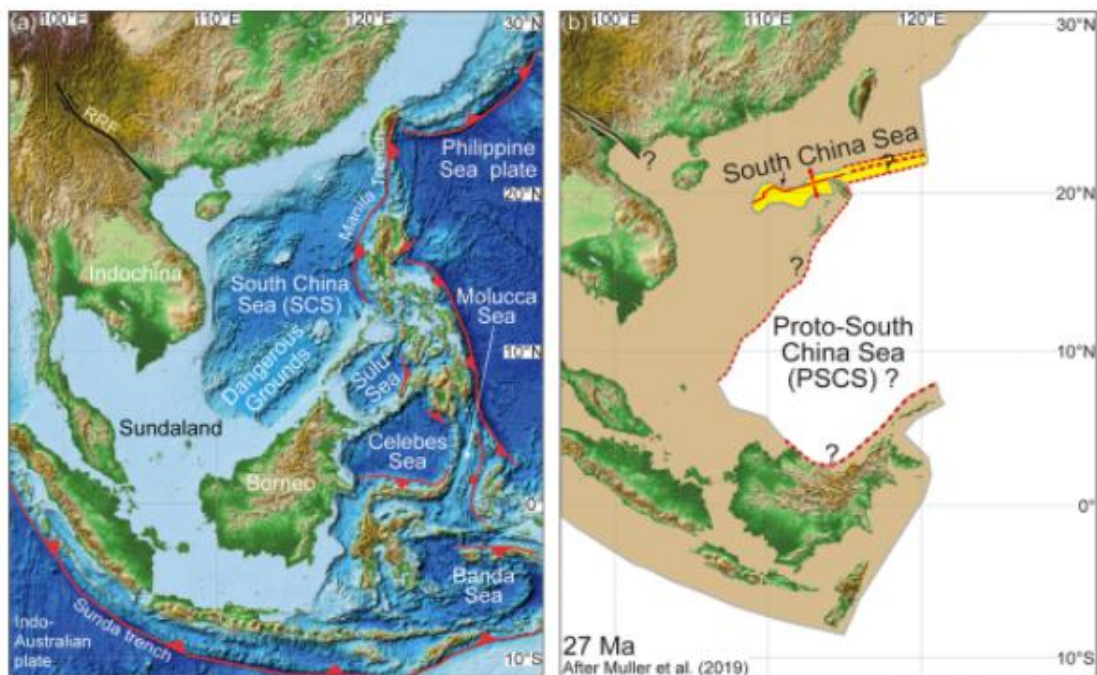
Figure 1. (a) Present-day tectonic setting of the South China Sea (SCS) and surrounding SE Asia after Hall (2012) and Cullen et al. (2012). Red lines indicate subduction zones and triangle teeth point to the overriding plate. (b) Plate reconstruction of SCS area during the Oligocene, prior to the main phase of SCS spreading (after Müller et al., 2019). The hypothesized proto-South China Sea (PSCS) ocean basin

is thought to have existed within the plate reconstruction gap (white areas) between the SCS and Borneo. RRF: Red River fault.
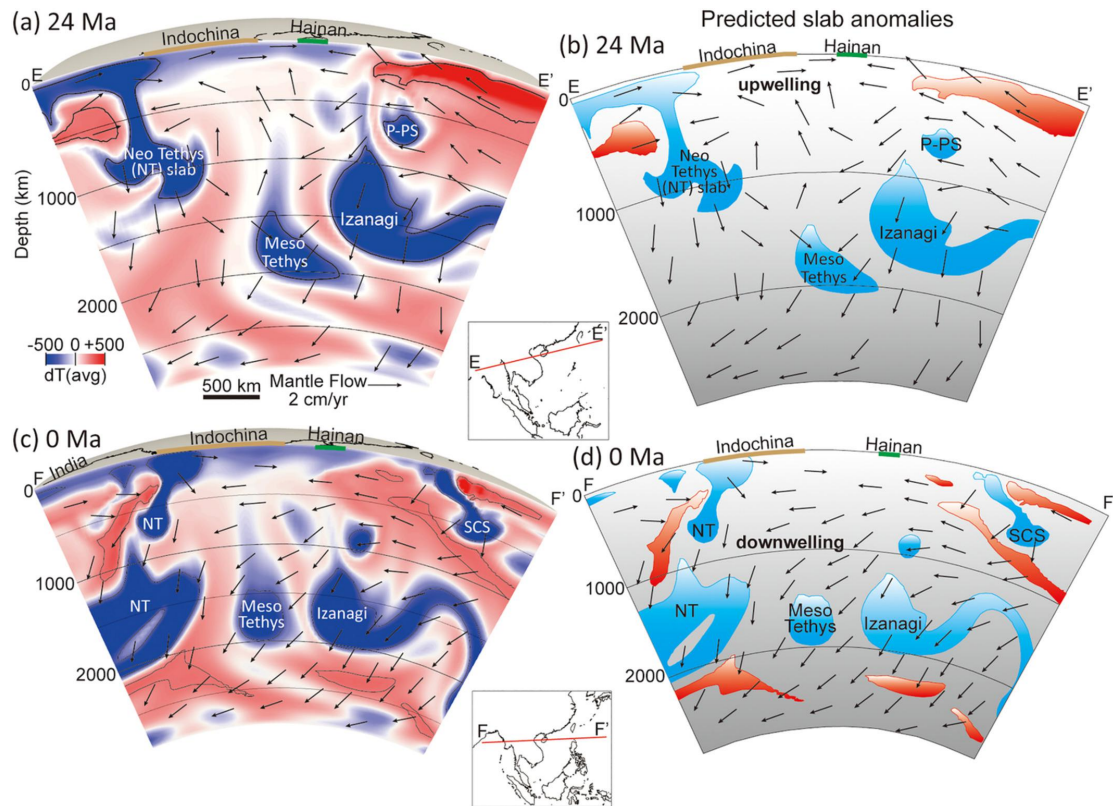
Figure 2. (a) and (b) Predicted mantle flows and mantle structures from our preferred geodynamic Model 2b under Indochina and Hainan Island during the latest Oligocene 24 Ma. (c) and (d) Present-day 0 Ma. From the late Eocene to Oligocene the model predicts a midmantle convective upwelling beneath Indochina and Hainan. At 0 Ma, the model predicts an extensive E-W directed mantle downwelling that is inconsistent with a deep-origin Hainan mantle plume. Black arrows show mantle flows and the black lines indicate the ± 300 °C temperature contours. The inset maps show reconstructed coastlines and cross-section locations at 24 Ma and the present-day.

8. 末次冰期日本海西北部千年尺度的环境变化

翻译人：杨会会 11849590@mail.sustech.edu.cn

摘要：通过对日本海西北海域的 LV 53-29 岩芯花粉和硅藻的高分辨率分析，本文追踪了过去 120 ka 的气候、植被和海洋变化。岩芯的年龄模型基于地质年代学、颜色明暗和磁化率。精准的年龄可用于与 Dansgaard-Oeschger 循环的对应。岩芯的孢粉和硅藻数据记录了东亚季风和海平面的海面升降的变化，以及海流方向和强度变化的影响。栓皮栎和柳杉花粉的增加反映了间冰期。柳杉的最大值出现在海洋同位素阶段(MIS) 5，与夏季季风强度的增加有关。华北落叶松的增加是冰期的标志，它出现在所有的海洋同位素阶段。硅藻记录的变化表明，日本海西北海域的海洋环境与其东部和南部海域不同。尽管盐度正常，海表水温比今天低，但冷水和多盐扶扶红的增加指示了间冰期。毛角动物属是冰期的特征，在 MIS 2 期间物种丰富。角毛藻的优势类群和硅藻的高总丰度可能反映了区域上升流。该时期半咸水物种的丰富指示了表水的轻微更新。对来自日本海西北部沉积物中的花粉、孢子和硅藻的研究表明，这些代用指标在识别高时间分辨率海洋记录中的气候突变方面具有巨大的潜力，特别是与冰期-间冰期有关的气候突变。

ABSTRACT: High-resolution analyses of pollen and diatoms in core LV 53-29 from the northwestern Japan Sea trace climate, vegetation and oceanographic changes during the past 120 ka. The age model for the core was based on tephrochronology, color lightness and magnetic susceptibility and was used to aid correlation with Dansgaard-Oeschger cycles (warm Greenland interstadials (GIs) and cold Greenland stadials (GSs)). The palynological and diatom data from this core record the changing influences of the East Asian monsoon, eustatic fluctuations in sea level, and the impact of variations in the direction and intensity of marine currents. Increases in *Quercus* and *Cryptomeria* pollen reflect GIs. The highest values of *Cryptomeria* were recorded

during Marine Isotope Stage (MIS) 5 and were associated with an increase in the intensity of the summer monsoon. The increase in *Larix* pollen is an indicator of GSs, and it occurs in all marine isotopic stages. Changes in diatom records indicate that oceanographic conditions in the northwestern Japan Sea differed from its southern and eastern regions. An increase in the cold-water and polyhalobous *Rhizosolenia hebetata* indicates GIs, although the surface water temperatures were colder than today with normal salinity. Species of the genus *Chaetoceros*, which is characteristic of GSs, were abundant during MIS 2. The predominance of *Chaetoceros* taxa and the high total abundance of diatoms may reflect regional upwelling conditions. The absence of brackish-water species at this time indicates a slight freshening of the surface water. The study of pollen, spores and diatoms in sediments from the northwestern Japan Sea illustrates the great potential of these proxies for identifying abrupt climate oscillations preserved in high-temporal resolution marine records, particularly those related to interstadial and stadial conditions.
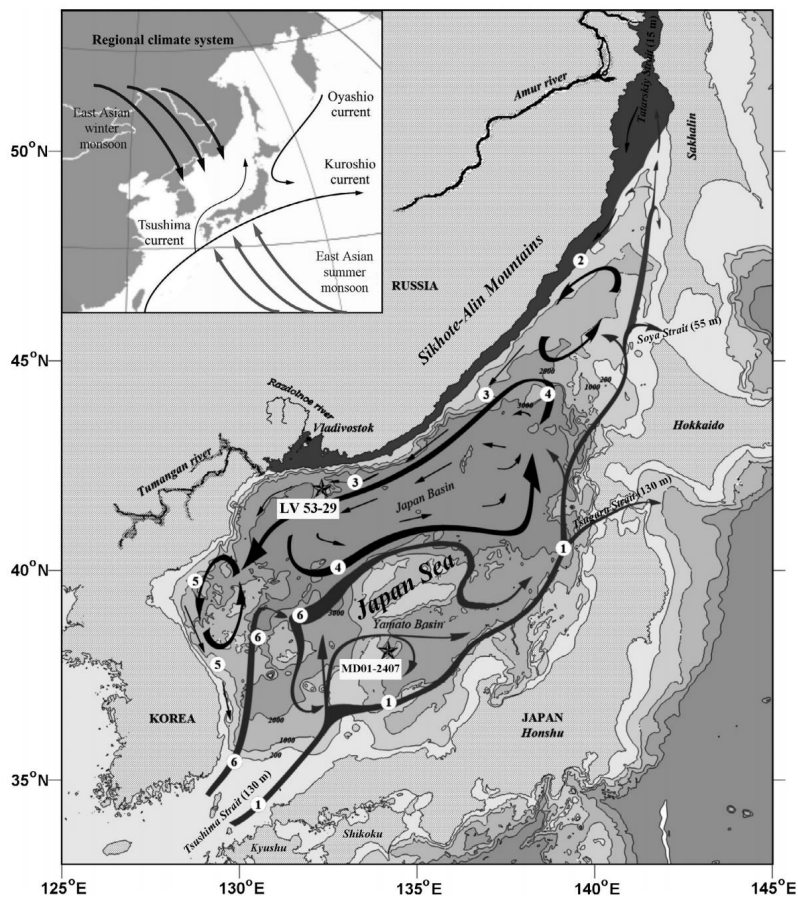
Figure 1. Map of the Japan Sea region. A star indicates the location of core LV 53-29. The marine

currents in the Japan Sea (Yarichin 1980) are (1) Tsushima Warm Current, (2) Shrenk Current, (3) Primorskoye (Liman) Current, (4) South Primorskoye Current, (5) North Korean Cold Current, and (6) East Korean Warm Current. The inset map shows the major regional climate systems with East Asian monsoon (black arrows = winter monsoon; grey arrows = summer monsoon) for the study area.
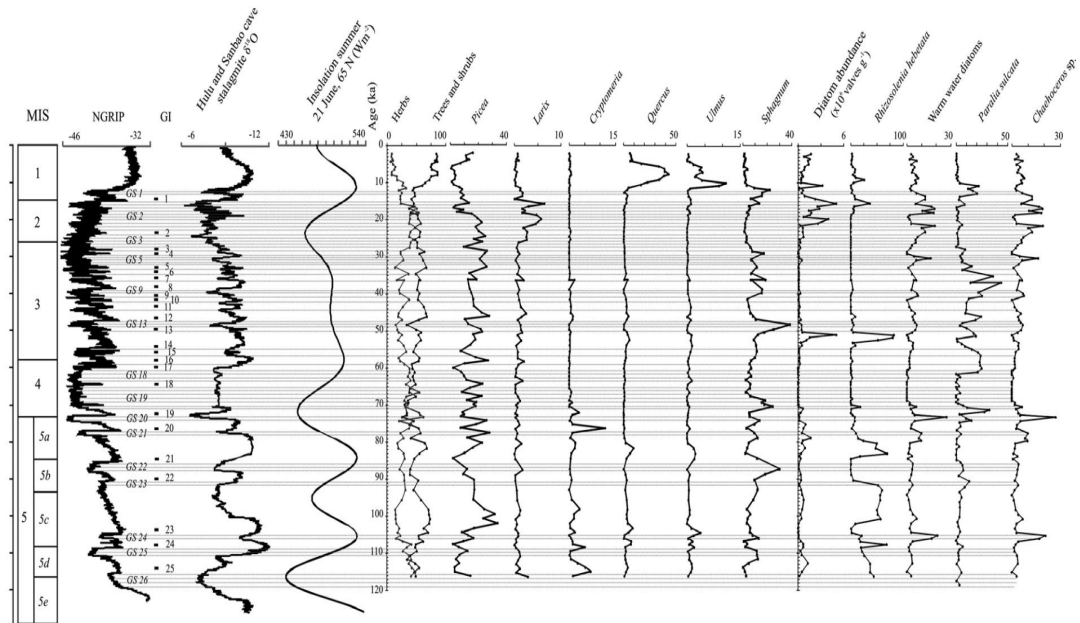
Figure 2. The relationship between the percentages of terrestrial pollen (herbs, trees and shrubs), diatom abundance (9106 valves g⁻¹ dry sediment), warm-water diatoms and selected indicator taxa from core LV 53-29 with NGRIP (North Greenland Ice Core Project Members 2004), selected Chinese stalagmite records from China (Wang et al. 2008) and summer insolation (Laskar et al. 2004). The dotted lines indicate GSs. The GS numbers always follow directly the GI number.

9. 西藏中部隆起的年代学修正（Lunpola Basin）

翻译人：曹伟 11930854@QQ.com

摘要：了解青藏高原的地形演化，对于理解青藏高原的结构及其对气候、环境和生物多样性的影响至关重要。根据西藏中部 Lunpola 盆地稳定同位素记录所估计的历史海拔高度，至少从 35 Ma 以来就形成了高原，但最近发现的低海拔热带化石明显沉积于 25.5 Ma，对过去研究提出了挑战。本研究中，我们使用磁性地层学和放射年代学方法来修正 Lunpola 盆地高程估算的年代约束。结果表明，39.5 Ma 时青藏高原中部海拔高度普遍较低(< 2.3 km)，~ 26 Ma 时较高(3.5-4.5 km)。这支持了始新世以来低海拔、纵向方向狭窄区域的存在，直到中新世早期它们发生抬升，这对青藏高原的生长机制、亚洲大气环流、地表过程和生物进化具有潜在影响。

ABSTRACT: Knowledge of the topographic evolution of the Tibetan Plateau is essential for understanding its construction and its influences on climate, environment, and biodiversity. Previous elevations estimated from stable isotope records from the Lunpola Basin in central Tibet, which indicate a high plateau since at least 35 Ma, are challenged by recent discoveries of low-elevation tropical fossils apparently deposited at 25.5 Ma. Here, we use magnetostratigraphic and radiochronologic dating to revise the chronology of elevation estimates from the Lunpola Basin. The updated ages reconcile previous results and indicate that the elevations of central Tibet were generally low (< 2.3 km) at 39.5 Ma and high (3.5 to 4.5 km) at ~ 26 Ma. This supports the existence in the Eocene of low-elevation longitudinally oriented narrow regions until their uplift in the early Miocene, with potential implications for the growth mechanisms of the Tibetan Plateau, Asian atmospheric circulation, surface processes, and biotic evolution.
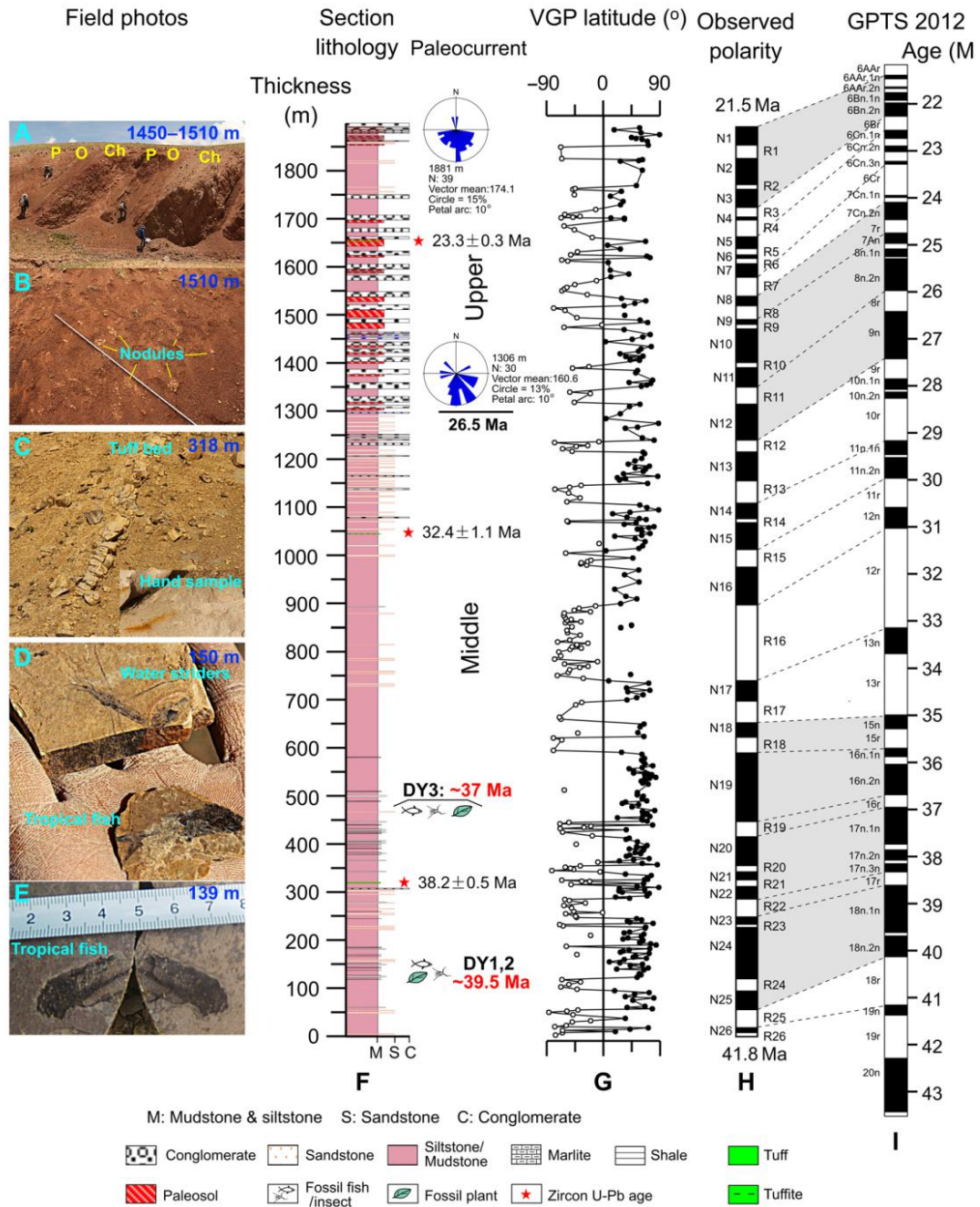
Figure 1. Correlation of the observed magnetic polarity zones of the measured Dayu section on the northern limb of the Dayu anticline with the geomagnetic polarity time scale based on tuff zircon U-Pb age constraints. (A) Paleosol complexes developed on the top of each cycle of channel deposition (conglomerates): overbank deposits (siltstones-mudstones) of a braided river environment. (B) Paleosol nodules in luvic paleosol complexes. (C) Tuff layer at the thickness of 318 m. (D) Tropical water striders and fish (climbing perch) found in shales at the thickness of 150 m. (E) Tropical fish (climbing perch) found in grayish shale at the thickness 139 m. (F) Schematic lithologic log of the composite

section showing stratigraphic positions of paleo-current measurements, radiogenic dating samples and fossils within the Middle and Upper members of the Niubao Formation. (G) Virtual Geomagnetic Pole latitudes from paleomagnetic samples throughout the section. Open (full) dots indicate reversed (normal) polarity directions. (H) Polarity zones (N for Normal and R for Reversed) inferred from VGP latitudes. Top and basal estimated ages are from correlations to the GPTS indicated by dashed lines to the panel I on the right. (I) Geomagnetic Polarity Time Scale. GPTS, geomagnetic polarity time scale.

10. E-O 转换期间大洋深层水，碳同位素和冰盖体积的演化

翻译人：王敦繁 dunfan-W@foxmail.com

摘要：利用底栖有孔虫配对的稳定同位素和 Mg/Ca 数据，估算了与始新世-渐新世过渡（EOT）相关的底水温（BWT）和冰量变化，这是过去 50 个百万年最大的全球气候事件。我们利用南大西洋的 ODP 站点 1090 和 1265 评估了 EOT（约 338 - 33.54 Ma）期间海水 $\delta^{18}O$（dw）、南极冰量和海平面变化。同时，利用底栖 $\delta^{13}C$ 数据重建了该地区海底水文过程中深水团的来源。我们的数据和以前发表的记录表明，在 EOT 之前和之后，一股北方成分的水冲击影响了南大西洋。底栖生物 $\delta^{18}O$ 记录显示，在 33.8 Ma（EOT-1）的温度升高 0.5‰，这代表了一个小的（约 10 m）的上升，然后在 Oi-1 的温度升高 1.0‰。在我们的 Mg/Ca 记录中，Oi-1（约 33.54 Ma）的预期深水降温并不明显。我们认为，碳酸盐岩饱和状态影响 Mg/Ca 数据的同时变化掩盖了冷却作用。为了解释这一点，根据最近发表的工作，冰体积的估计进行了修正。在 1090 和 1265 位点，修正后的 BWT 显示出与 Oi-1 一致的 1.5°C 的降温，平均增加约 0.75‰，冰量的增加导致全球海平面下降约 70 米，南极冰原的大小接近现代或略大。

ABSTRACT: Paired benthic foraminiferal stable isotope and Mg/Ca data are used to estimate bottom water temperature (BWT) and ice volume changes associated with the Eocene-Oligocene Transition (EOT), the largest global climate event of the past 50 Myr. We utilized ODP Sites 1090 and 1265 in the South Atlantic to assess seawater $\delta^{18}O$ (dw), Antarctic ice volume, and sea level changes across the EOT (~ 33.8–33.54 Ma). We also use benthic $\delta^{13}C$ data to reconstruct the sources of the deep water masses in this region during the EOT. Our data, together with previously published records, indicate that a pulse of Northern Component Water influenced the South Atlantic immediately prior to and following the EOT. Benthic $\delta^{18}O$ records show a 0.5‰ increase

at ~ 33.8 Ma (EOT-1) that represents a ~ 2°C cooling and a small (~ 10 m) eustatic fall that is followed by a 1.0‰ increase associated with Oi-1. The expected cooling of deep waters at Oi-1 (~ 33.54 Ma) is not apparent in our Mg/Ca records. We suggest the cooling is masked by coeval changes in the carbonate saturation state (D[CO^{2-}]) which affect the Mg/Ca data. To account for this, the 3 BWT, ice volume, and d estimates are corrected for a change in the D[CO^{2-}] of deep w3 waters on the basis of recently published work. Corrected BWT at Sites 1090 and 1265 show a ~ 1.5°C cooling coincident with Oi-1 and an average dw increase of ~ 0.75‰. The increase in ice volume during Oi-1 resulted in a ~ 70 m drop in global sea level and the development of an Antarctic ice sheet that was near modern size or slightly larger.
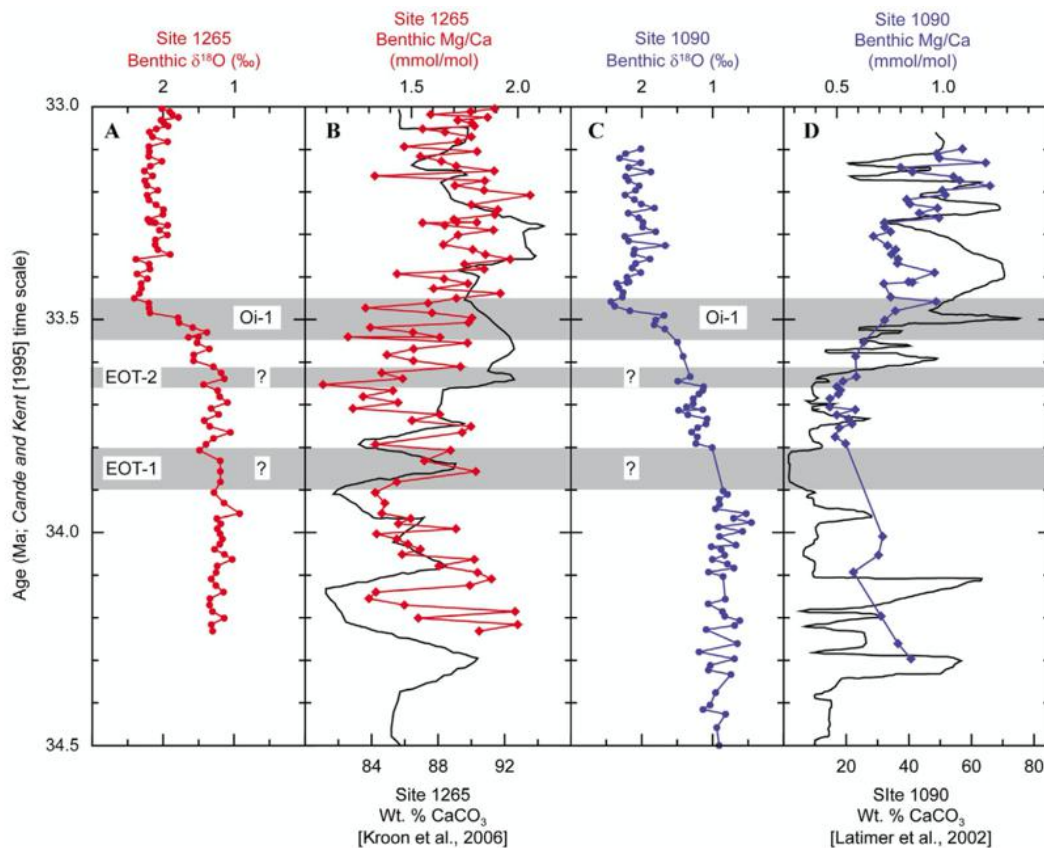
Figure 1. ODP Sites 1265 and 1090 benthic foraminiferal δ18O, Mg/Ca, and weight percent carbonate records verses age in millions of years. (a) Site 1265 benthic foraminiferal δ18O values (red circles; Cibicidoides spp.) verses age in millions of years. Isotope values are reported relative to the VPDB (Vienna PeeDee belemnite) standard. (b) Site 1265 benthic foraminiferal Mg/Ca ratios (red diamonds; C. praemundulus) in mmol/mol plotted with weight percent carbonate (black line) from Kroon et al.

[2006]. (c) Site 1090 benthic foraminiferal $\delta^{18}O$ values (blue circles; Cibicidoides spp.). (d) Site 1090 benthic foraminiferal Mg/Ca ratios (blue diamonds; Cibicidoides spp.) in mmol/mol plotted with weight percent carbonate (black line) from Latimer and Filippelli [2002]. Gray bars mark the EOT-1 (Eocene-Oligocene transition event 1), EOT-2 (Eocene-Oligocene transition event 2), and Oi-1 (Oligocene isotope event 1) events occurring at 33.8, 33.63, and 33.54 Ma, respectively [Miller et al., 1991, 2008; Lear et al., 2004; Coxall et al., 2005; Katz et al., 2008].

11. 以非洲阿拉伯大火成岩省的推断约 30 Ma 的地磁场古强度

翻译人：王浩森 11930841@mail.sustech.edu.cn

摘要：格陵兰岛的冰期和间冰期（GS 和 GIS）是上个冰期冰芯记录中的突出特征，其特征是千年尺度的气候振荡以及年代际的水文气候变化。在过去的二十年中，对中国石笋记录的研究揭示了相应的中国冰期/间冰期（CS / CIS）。但是，对 CS / CIS 的转变及其在亚洲季风地区的相应驱动机制仍未完全了解。在这项研究中，我们提出了来自中国东南部仙云洞的基于 ^{230}Th 年代际高精度的石笋 δ^{18}O 记录，涵盖了 58.2-50.8 kyr（1950 年之前）时期，包括 GIS（和 CIS）16-14。我们将年代学中 GIS（CIS）15.1（峰值）和 15.2（第一个点）与高低纬度记录进行比对发现，我们记录中 GIS 14 的发生早于格陵兰的冰芯记录和中国北方的石笋记录。这一发现表明，低纬度热带气候可能在引发突然的千年尺度事件中起了关键作用。此外，在我们的记录中，向 GIS 14 的过渡时期持续了 1.49 千年，这与 NGRIP 中观测到的温度快速上升形成了对比。与以前的石笋记录相比，我们确定了季风中国进入 GIS 14 的两种过渡模式：1）中国北方的快速过渡和 2）中国东南部的逐步过渡。在仙云记录中的逐渐过渡类似于西部热带太平洋的海表温度（SST）记录，突显了西部热带太平洋 SST 的变化与中国东南部的东亚夏季风变化之间可能存在内在联系。因此，中国东南部的古气候记录对于理解突然的千年尺度气候事件的机制至关重要，因为它们可以作为高纬度和低纬度记录之间的桥梁。

ABSTRACT: Greenland stadials and interstadials (GS and GIS) are prominent features in ice core records of the last glacial period and are characterized by millennial-scale climate oscillations with sub decadal- to decadal-scale hydroclimatic shifts. Over the past two decades, studies of Chinese stalagmite records have revealed corresponding Chinese Stadials/Interstadials (CS/CIS).

However, the CS/CIS shifts and their corresponding forcings across the Asian monsoon region are still not fully understood. In this study, we present a 230Th-based sub-decadally-resolved stalagmite $\delta^{18}O$ record from Xianyun Cave in southeastern China covering the period 58.2-50.8 kyr BP (before 1950 AD) and including GIS (and CIS) 16-14. We used GIS (CIS) 15.1 (peak point) and 15.2 (first point) to chronologically link the high and low-latitude records. We found that the onset of GIS 14 in our record occurred earlier than in an ice core record from Greenland and stalagmite records from northern China. This finding implies that low latitude tropical climate likely played a key role in triggering abrupt millennial-scale events. Moreover, the transition into GIS 14 lasted 1.49 kyr in our record, which is in contrast to the abrupt temperature rise observed in NGRIP (the North Greenland Ice Core Project, 0.02 kyr). Compared with previous stalagmite records, we identified two transitional patterns into GIS 14 in monsoonal China: 1) a rapid transition in northern China and 2) a gradual transition in southeastern China. The gradual transition in our Xianyun record is analogous to a sea surface temperature (SST) record in the western tropical Pacific, highlighting a possible inherent connection between the changes in western tropical Pacific SSTs and East Asian summer monsoon variability in southeastern China. Paleoclimate records in southeastern China are therefore critical for understanding the mechanisms of abrupt millennial-scale climate events, as they can act as a bridge between high- and low-latitude records.
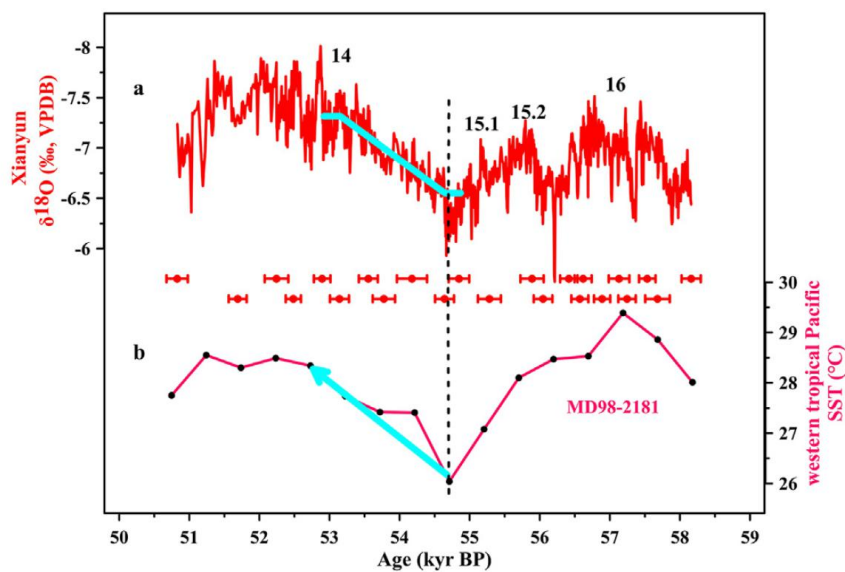
Figure 1. Comparison of $\delta^{18}O$ records between (a) Xianyun Cave (red; this study), (b) SST in the

western tropical Pacific (neon red; Stott et al., 2002). Black dashed line denotes the onset of GIS 14. Cyan line/arrow denote the trend into GIS 14. (For interpretation of the references to color in this figure legend, the reader is referred to theWeb version ofthis article.)

12. 全球人造物质量超过生物总质量

翻译人：郑威　11930589@mail.sustech.edu.cn

摘要：人类已经成为塑造地球表面形态的主导力量。浮现而出的一个问题就是人类活动产生的物质总和与自然生物物质相较若何？在这里，我们量化了人造物质质量（人为质量），并将其与约为1.1个teratonnes的地球生物总质量进行比较。我们发现地球正好在2020（±6）年处于交点上，人为质量最近大约每20年就翻一倍，将会超过全球生物总质量。平均而言，地球上每个人每周都会产生超过自己体重的人为质量。这个对人类事业的量化给出了人类世人为介入时代的基于质量的定量化和符号化特征。

ABSTRACT: Humanity has become a dominant force in shaping the face of Earth[1,2,3,4,5,6,7,8,9]. An emerging question is how the overall material output of human activities compares to the overall natural biomass. Here we quantify the human-made mass, referred to as 'anthropogenic mass', and compare it to the overall living biomass on Earth, which currently equals approximately 1.1 teratonnes[10,11]. We find that Earth is exactly at the crossover point; in the year 2020 (± 6), the anthropogenic mass, which has recently doubled roughly every 20 years, will surpass all global living biomass. On average, for each person on the globe, anthropogenic mass equal to more than his or her bodyweight is produced every week. This quantification of the human enterprise gives a mass-based quantitative and symbolic characterization of the human-induced epoch of the Anthropocene.
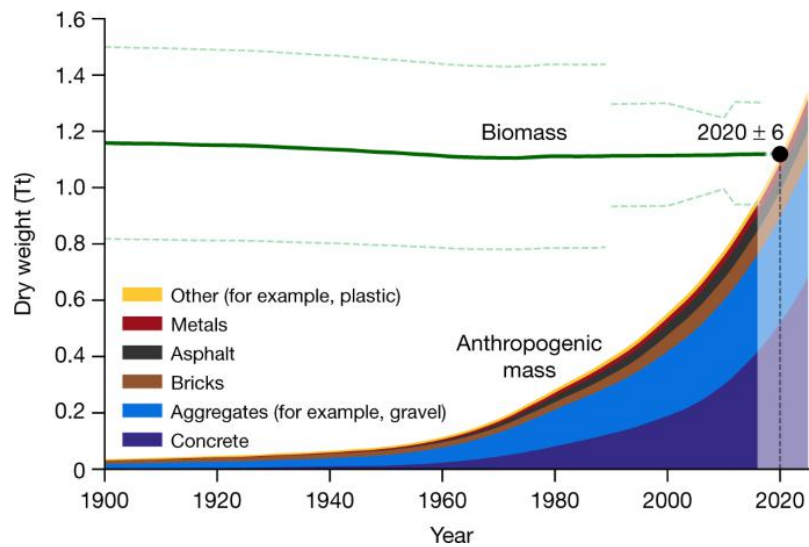
Figure 1. The green line shows the total weight of the biomass (dashed green lines, ±1 s.d.). Anthropogenic mass weight is plotted as an area chart, where the heights of the coloured areas represent the mass of the corresponding category accumulated until that year. The anthropogenic mass presented here is grouped into six major categories. The year 2020 ± 6 marks the time at which biomass is exceeded by anthropogenic mass. Anthropogenic mass data since 1900 were obtained from ref. [22], at a single-year resolution. The current biomass value is based on ref. [11], which for plants relies on the estimate of ref. [10], which updates earlier, mostly higher estimates. The uncertainty of the year of intersection was derived using a Monte Carlo simulation, with 10,000 repeats (see Methods). Data were extrapolated for the years 2015–2025 (lighter area; see Methods). For a detailed view of the stock accumulation for the 'metals' and 'other' groups, see Extended Data Figs. [4,5].

13. 黄河口和莱州湾表层沉积物的磁学性质对重金属监测的意义

翻译人：李海 12031330@mail.sustech.edu.cn

摘要： 黄河口及其邻近的莱州湾面临重金属污染带来的生态环境风险。为此，对来自黄河口和莱州湾的239个表层沉积物样品进行磁性测量，以建立一种快速有效的方法来检测重金属。沉积物主要由磁铁矿、磁赤铁矿和赤铁矿组成。沉积物的分布主要受沉积物源以及逆时针水流控制。相较于背景值，所有样品中的均富集Cd，而大多数样品中的Co、Cr、Ni、Cu、Zn和Pb含量较低。重金属的污染负荷指数（PLI）表示未污染到中度污染状态，泥质区污染最严重。主成分分析结果表明：Co、Cr、Ni、Cu和Zn主要来自自然风化物质，而Cd和Pb是人为来源。细颗粒沉积物和磁性颗粒的含量与Co、Ni、Cu、Zn和PLI正相关。通过频率磁化率可以快速圈定Co、Ni、Cu和Zn的高风险区域。

ABSTRACT: The Yellow River Estuary (YRE) and adjacent Laizhou Bay (LB) encounter eco-environmental risks caused by heavy metals (HMs) pollution. Here magnetic measurements were performed on 239 surface sediment samples from the YRE and LB to establish a rapid and effective method for detecting HMs. Magnetite, maghemite, and hematite coexist in the sediments. The distributions of magnetic minerals are dominated by sediment sources (Yellow River in northern and western LB, and rivers in southern and eastern coastal LB), and the anticlockwise water current. Compared to the background values, Cd content is enriched for all samples, while Co, Cr, Ni, Cu, Zn, and Pb contents are lower for most samples. The low pollution load indexes (PLI) of HMs (< 1-1.56) indicate the unpolluted to moderately polluted status, while the muddy area is the most polluted. The principal component analysis indicates that Co, Cr, Ni, Cu, and Zn are mainly from natural weathering substances, while Cd and Pb are anthropogenic. Contents of

fine-grained sediments and magnetic particles are positively correlated to Co, Ni, Cu, Zn, and PLI. The high-risk Co, Ni, Cu, and Zn regions can be quickly delineated with the frequency-dependent susceptibility.
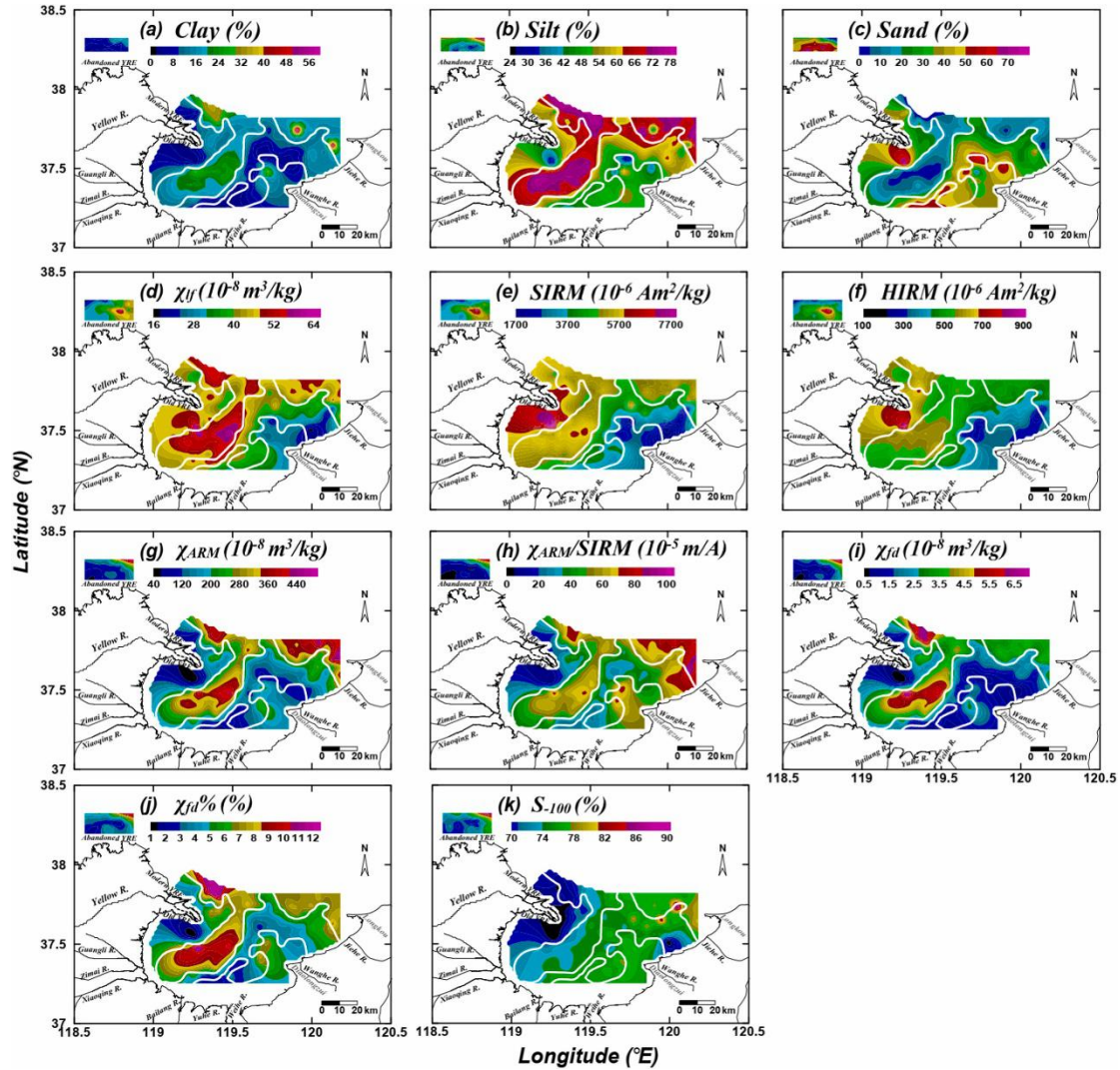
Figure 1. Contour maps of (a) clay (%), (b) silt (%), (c) sand (%), (d) χ_{lf} (10^{-8} m³/kg), (e) SIRM (10^{-6} Am²/kg), (f) HIRM (10^{-6} Am²/kg), (g) χ_{ARM} (10^{-8} m³/kg), (h) χ_{ARM}/SIRM (10^{-5} m/A), (i) χ_{fd} (10^{-8} m³/kg), (j) χ_{fd}% (%), and (k) S$_{-100}$ (%).

14. 测试沉积岩古地磁数据在古地理重建中的可靠性

翻译人：张伟杰 12031188@mail.sustech.edu.cn

摘要：古地理重建在很大程度上依赖于古地磁资料，主要以古地磁极的形式进行。视极移曲线一系列地磁极的综合解释来确定，它能捕捉特定位置相对于绝对参考系(如地球的自转轴)的时间运动。由于沉积岩的空间分布和时间连续性，古地磁数据集具有特别的相关性。多年来，人们提出了几个评价古地磁数据可靠性的标准。其中，一个被广泛接受的古长期变化模型所预测的依赖于纬度拉长的给定古地磁方向分布，目前仅用于研究沉积岩中常见的倾角浅化现象。本文的工作表明，这一概念可以推广到由构造应变产生的古地磁污染的检测中，而这种污染往往不能仅通过野外观测来检测。在不同纬度上生成不同组的模拟地磁方向后，我们在应用变形张量来复制分布的构造应变的影响之后，监测了分布形状的变化。研究表明，在大多数情况下，数据集的变形可以通过不符合古长期变化模型预测值的伸长率与倾角比值来检测。最近从新喀里多尼亚获得的古地磁方向和磁化率各向异性数据验证了这些模拟结果，并强调了利用沉积古地磁数据重建古地理时测量 AMS 的重要性。建议在沉积古地磁资料的古地理重建中，应始终包括 AMS 测量和分布形态分析。

ABSTRACT: Paleogeographic reconstructions largely rely on paleomagnetic data, mostly in the form of paleomagnetic poles. Compilations of poles are used to determine so called apparent polar wander paths (APWPs), which capture the motion through time of a particular location with respect to an absolute reference frame such as the Earth's spin axis. Paleomagnetic datasets from sedimentary rocks are particularly relevant, because of their spatial distribution and temporal continuity. Several criteria have been proposed through the years to assess the reliability of paleomagnetic datasets. Among these, the latitudinal-dependent elongation of a given

paleomagnetic directions distribution, predicted by a widely accepted paleosecular variations model, has been applied so far only to investigate inclination flattening commonly observed in sedimentary rocks. We show in this work that this concept can be generalized to detect "contamination" of paleomagnetic data derived from tectonic strain, which is not always detected by field observation only. After generating different sets of simulated geomagnetic directions at different latitudes, we monitored the variations in the shape of the distributions after applying deformation tensors that replicate the effect of increasing tectonic strain. We show that, in most cases, the "deformation" of the dataset can be detected by elongation vs. inclination ratios not conforming to the values predicted by the paleosecular variations model. Recently acquired paleomagnetic directions and anisotropy of magnetic susceptibility (AMS; a parameter very sensitive to tectonic strain) data from New Caledonia verifies the results of these simulations and highlights the importance of measuring AMS when using sedimentary paleomagnetic data for paleogeographic reconstruction. We suggest to include always AMS measurement and analysis of the distribution shape to assess sedimentary paleomagnetic data used for paleogeographic reconstructions.
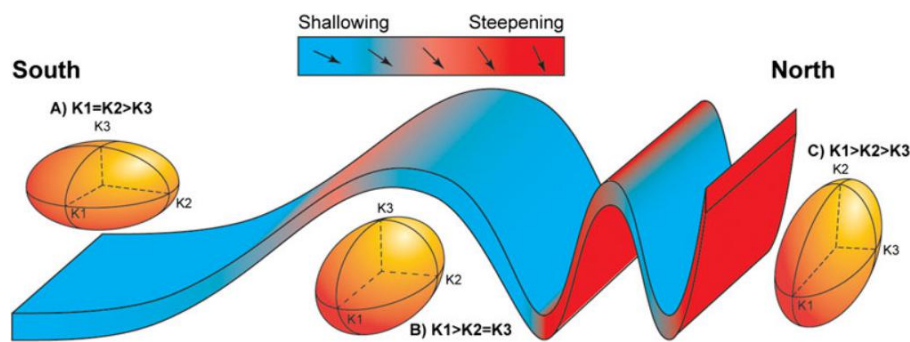
Figure 1. Theoretical evolution of magnetic fabric in sedimentary rocks during incipient deformation. (A) Absence of finite strain results in the solely effect of compaction-derived oblate fabric. (B) During a weak cleavage stage the fabric assumes a prolate shape, with the major axis perpendicular to the shortening direction. (C) In a strong cleavage state the fabric is triaxial, with the minor and major axes respectively parallel and perpendicular to the shortening direction. The effect of the fabric evolution on the paleomagnetic inclintaion is shown on top of the figure; figure drawn adapting concepts from Parés et al., 1999 and Borradaile, 1997.
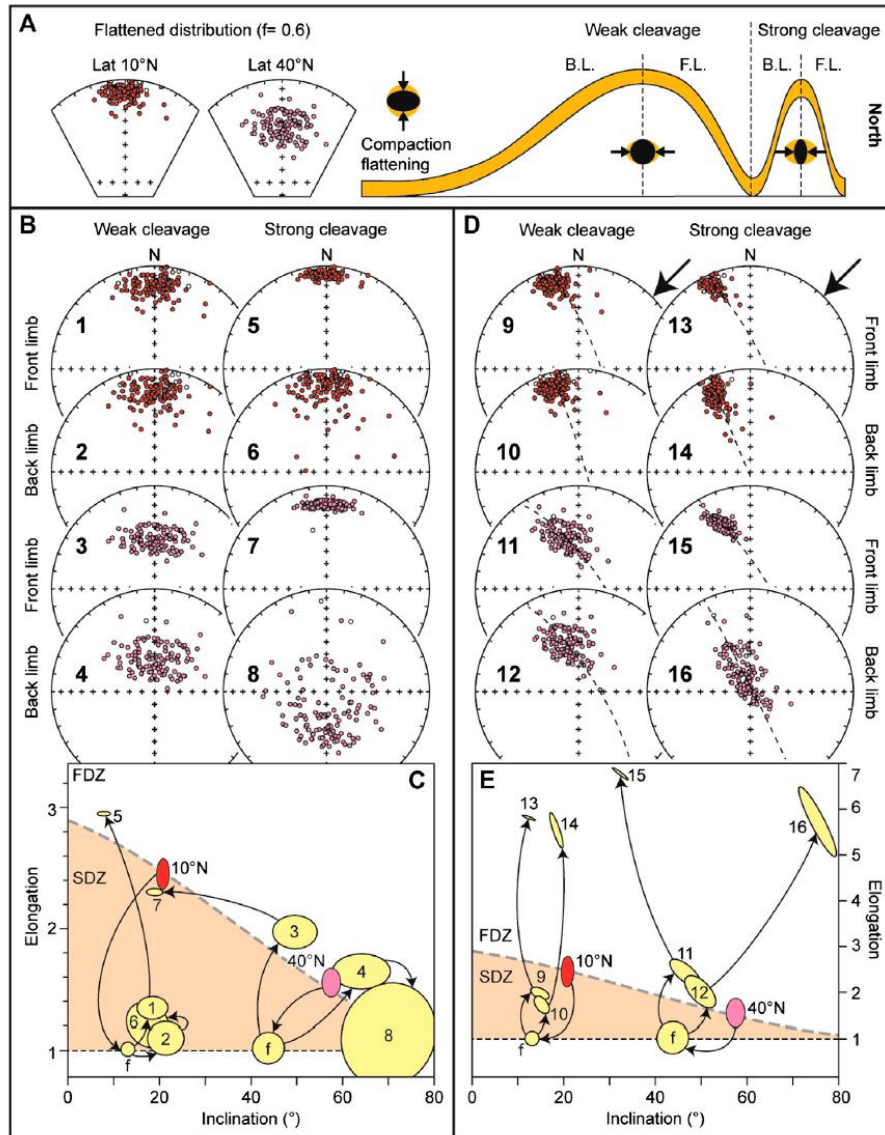
Figure 2. Effect of the strain simulation with strata tilting. (A) Two reference TK03.GAD distributions generated for a 10 and 40°N latitude are first subjected to inclination shallowing as described in the text; to the right hand side the conceptual model of the theoretical weak cleavage and strong cleavage conditions is shown on both the back limb (B.L.) and front limb (F.L.) of a fold system. (B) Effect of the different strain simulation on the two distributions as described in the main text; the bold numbers correspond to the ellipses shown in panel C. (C) Elongation vs. inclination of the data shown in panel B; data are shown together with the reference curve expected by the TK03.GAD model (dashed line), on which the original 10°N latitude (red) and the 40°N latitude (pink) sets lie; the dotted line is the minimum possible value of E (1 = circle); SDZ and FDZ = shallowed and flawed distribution zone, respectively. (D) and (E) are as B and C, but with a simulated shortening direction (minimum axis of the S matrix) oriented NE-SW.

15. 冰期南大洋碳储库异质性由南印度洋快速的释放而降低

翻译人：张亚南 zhangyn3@mail.sustech.edu.cn

摘要：过去大洋 ^{14}C 失衡的变化被认为是反映南大洋对全球外生碳循环的控制。然而，冰期碳库的体积范围和有助于冰消期沉积碳释放的机制，仍然缺乏足够的约束。我们用比小于常规的有孔虫样品开展的高分辨率 ^{14}C 测年和多指标深海氧化还原条件的评估，重建了科尔格伦群岛附近南印度洋上升流在冰消期的通风演化历史。我们发现南大洋翻转流显著的区域差异，在冰消期早期大气 CO_2 变化期间具有明显的南印度洋特征。这种非均质性的减弱开始于 14.6 kyr，标志着类现代的、强烈的南印度洋上升流的形成，可能受到大西洋翻转流增强的影响。我们的研究结果强调了南印度洋影响大气 CO_2 含量的能力，并放大了百年和千年尺度上半球间气候变化对全球碳循环的影响。

ABSTRACT: Past changes in ocean ^{14}C disequilibria have been suggested to reflect the Southern Ocean control on global exogenic carbon cycling. Yet, the volumetric extent of the glacial carbon pool and the deglacial mechanisms contributing to release remineralized carbon, particularly from regions with enhanced mixing today, remain insufficiently constrained. Here, we reconstruct the deglacial ventilation history of the South Indian upwelling hotspot near Kerguelen Island, using high-resolution ^{14}C-dating of smaller-than-conventional foraminiferal samples and multi-proxy deep-ocean oxygen estimates. We find marked regional differences in Southern Ocean overturning with distinct South Indian fingerprints on (early de-)glacial atmospheric CO_2 change. The dissipation of this heterogeneity commenced 14.6 kyr ago, signaling the onset of modern-like, strong South Indian Ocean upwelling, likely promoted by rejuvenated Atlantic overturning. Our findings highlight the South Indian Ocean's capacity to influence atmospheric CO_2 levels and

amplify the impacts of inter-hemispheric climate variability on global carbon cycling within centuries and millennia.
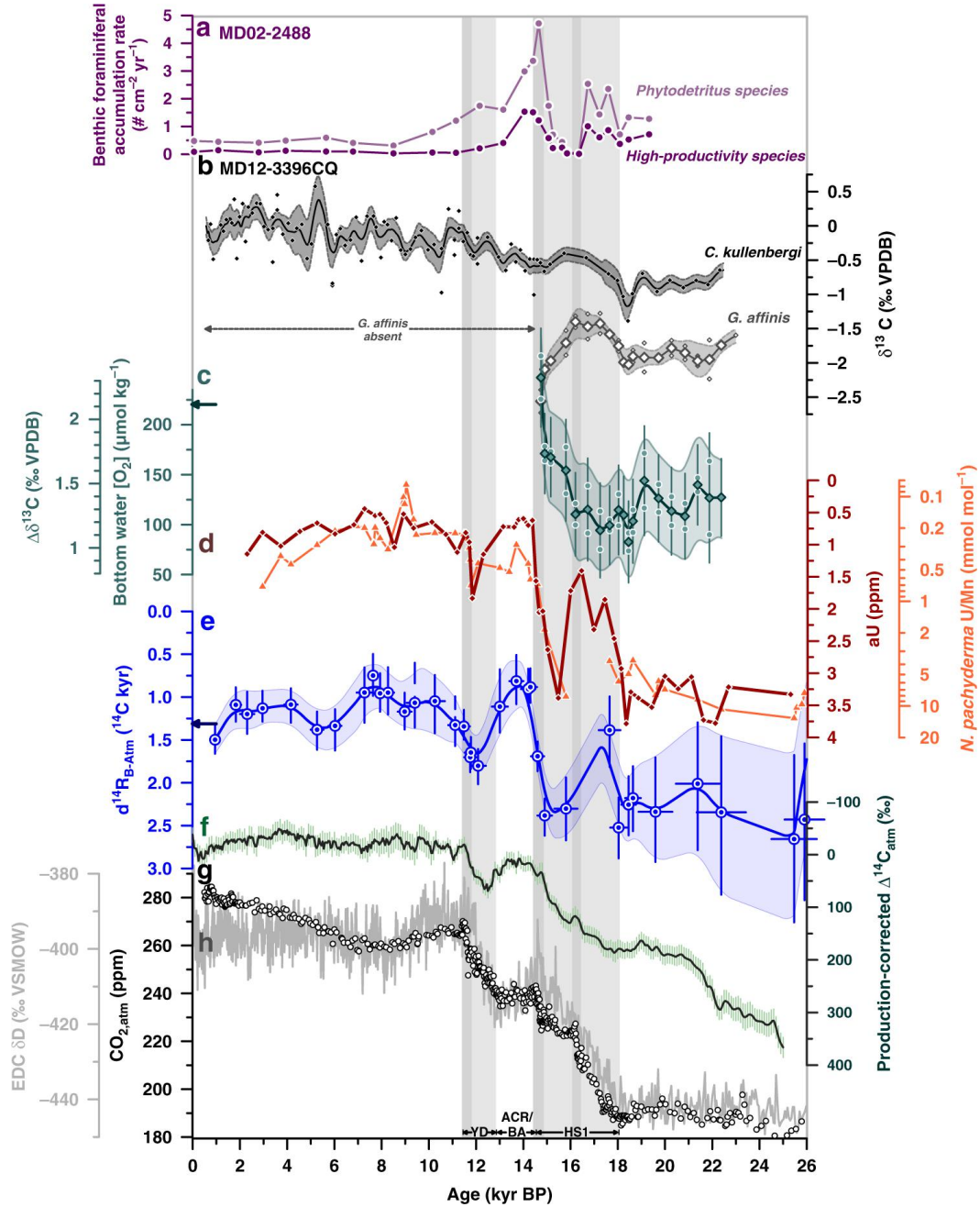
Figure 1. Deglacial oxygenation and deep-ocean reservoir age variations in the South Indian Ocean. a Accumulation rates of benthic foraminifera indicative of phytodetrital input (light purple) and high annual productivity (dark purple) in core MD02-2488, b benthic foraminiferal $\delta^{13}C$ records from MD12-3396CQ (black (epibenthic/shallow infaunal species): *Cibicides kullenbergi*, grey (deep infaunal species): *Globobulimina affinis*; small symbols: replicate analyses, large symbols: mean

values), c δ^{13}C gradient between *G. affinis* and *C. kullenbergi* (Δδ^{13}C), and corresponding bottom water [O$_2$] levels at our study site (arrow indicates present-day bottom water [O$_2$]; small circles show the Δδ^{13}C range based on non-averaged *G. affinis* δ^{13}C values), diamonds show average values, d authigenic U (aU) levels (brown) and U/Mn ratios in authigenic coatings of *N. pachyderma* (orange) in MD12-3396CQ, e d[14]R$_{B-Atm}$ variations (arrow shows prebomb values, following the Global Ocean Data Analysis Project database, version 2) measured in core MD12-3396CQ, f production-corrected variations in Δ^{14}C$_{atm}$, g atmospheric CO$_2$ (CO$_{2,atm}$) variations (circles), and h EPICA Dome C (EDC) δD changes (grey line). Vertical bars indicate intervals of rising CO$_{2,atm}$ levels. Darker bands highlight periods with centennial-scale CO$_{2,atm}$ increases. Lines and envelopes in b, c and e show 0.5 kyr-running averages and the 1σ-uncertainty/66%-probability range, respectively. HS1 Heinrich Stadial 1, ACR Antarctic Cold Reversal, BA Bølling Allerød, YD Younger Dryas.
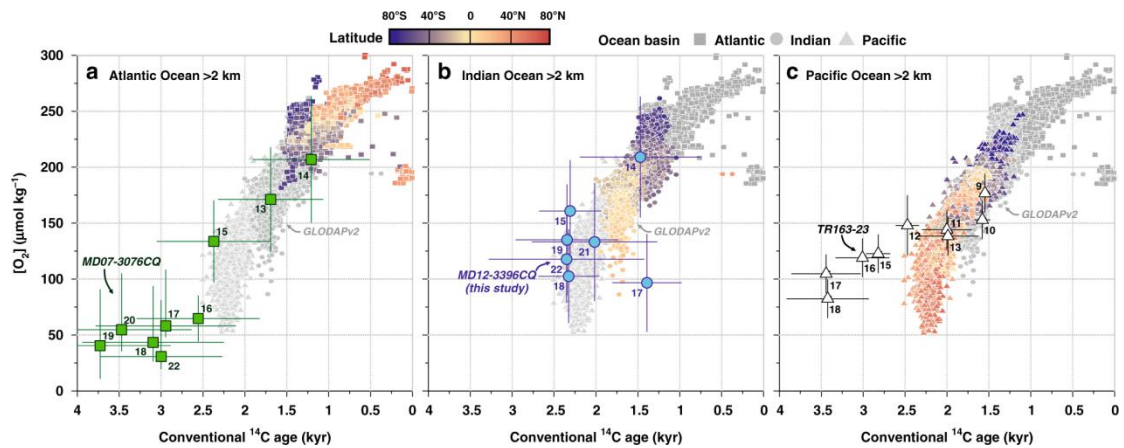
Figure 2. Relationship between seawater oxygen concentrations and conventional radiocarbon ages at present-day and in the past. Modern seawater [O$_2$] levels versus conventional ^{14}C age in a the Atlantic Ocean (squares), b Indian Ocean (circles), and c Pacific Ocean (triangles) below 2 km water depth; modified after ref. 4. Symbol color represents the latitude of the seawater sample. Large symbols show reconstructed bottom water [O$_2$] (via the Δδ^{13}C proxy) and ventilation ages (i.e. d[14]R$_{B-Atm}$, representing paleo-conventional ^{14}C ages) from the deep South Atlantic (green: MD07-3076CQ, 3.8-km water depth), the deep South Indian (blue, this study: MD12-3396CQ, 3.6-km water depth) and the deep Eastern Equatorial Pacific Ocean (black: sediment core TR163-23, 2.7 km water depth; please note that Holocene Δδ^{13}C proxy data in this core overestimate present-day bottom water [O$_2$] in the study region by ~80 µmol kg^{-1}). Symbol labels indicate temporal bins over which the paleo-[14]C-[O$_2$] data were

averaged (in kyr before present (BP), e.g. for 15 kyr BP: 15.99–15 kyr BP). The principal trend of increasing ventilation ages with decreasing seawater oxygen content can be ascribed to the accumulation of respired carbon, while deviations from this trend can be driven by the advection of well-ventilated water masses, e.g. from the Weddell Sea ([O_2] increase without ^{14}C change), or through organic carbon respiration in upwelling regions ([O_2] decrease without ^{14}C change). On multi-millennial timescales, the respiration rate may change (causing the [14]C-[O_2] slope to steepen or flatten), and the ocean-atmosphere ^{14}C and O_2 equilibration timescales change with varying atmospheric CO_2 levels (i.e. mean reservoir ages increase in a glacial 190 ppm-CO_2 atmosphere without [O_2] change) and ocean temperature/salinity (i.e. [O_2] saturation increases without ^{14}C change during glacials).